# Application of Solidification Theory to

## Rapid Solidification Processing

W. J. Boettinger, J. W. Cahn, S. R. Coriell,
J. R. Manning, and R. J. Schaefer
Metallurgy Division
Center for Materials Science
National Bureau of Standards
Washington, DC  20234

"The views and conclusions contained in this document
are those of the authors and should not be interpreted
as representing the official policies, either expressed
or implied, of the Defense Advanced Research Projects
Agency or the U.S. Government."

*A04526*
*In-House Lab.*

83  12  19  042

# Table of Contents

Accession For

| Accession For | |
|---|---|
| NTIS GRA&I | ☒ |
| DTIC TAB | ☐ |
| Unannounced | ☐ |
| Justification | |

By Per Ltr. on File

Distribution/

Availability Codes

| Dist | Avail and/or Special |
|---|---|
| A/1 | |

DTIC COPY INSPECTED 3

# APPLICATION OF SOLIDIFICATION THEORY TO
# RAPID SOLIDIFICATION PROCESSING

## Technical Report Summary

This semi-annual technical report for ARPA Order 3751 covers the period April 1, 1982 to September 30, 1982. Significant accomplishment during that period were achieved in the following areas:

## Extended Solid Solubilities - for Production of Alloys with New Compositions and Phases

o   The types of microstructures obtainable from rapid solidification of Ag-Cu alloys over the full range of alloy compositions from 1 wt% Cu up to the eutectic composition, 28.1 wt% Cu, were systematically determined.

o   Over this composition range, four general types of microstructure were found, depending on the composition and on the scan velocity of the electron beam system used to produce the rapid solidification. The scan velocity is closely related to the solidification velocity. Each of the four types of microstructure, (1) dendritic (cellular), (2) eutectic, (3) banded, and (4) micro-segregation-free, was found in a distinct region on a plot of alloy composition vs. scan velocity.

o   The appearance of a micro-segregation-free region on this plot and its extension across the entire composition range were related to morphological stability theory, to theories of solute trapping as a function of solidification velocity, and to phase diagram features, such as the $T_0$ curve.

o   The importance of considering the full metastable phase diagram in analysis of rapid solidification processes and resulting alloy microstructures was demonstrated.

1

## Solidification Interface Stability and Alloy Segregation - for Production of Improved Alloy Properties by Control of Microstructures and Homogeneity in Rapidly Solidified Alloys

o  In the equilibrium solubility range in Ag-Cu (less than 8% Cu), the critical solidification velocities above which planar, instead of cellular, solidification is obtained were predicted from theory. These predictions were confirmed by experiment.

o  Interface stability theory was generalized to allow for the velocity v dependence of the solute distribution coefficient k, thus including non-equilibrium effects.

o  For sufficiently large values of $(\partial k/\partial v)$ it was shown that interface instabilities which are oscillatory in time and which lead to three-dimensional segregation patterns can occur.

## Surface Effects -- for Production of Improved Alloy Surfaces by Rapid Solidification

o  The critical role of convective mixing in homogenization of surface melted and rapidly resolidified surface areas was evaluated.

o  A band of aluminum-copper eutectic alloy was produced on the surface of pure aluminum by pressing a copper wire into the surface and heating above the eutectic temperature. Convective mixing of the alloy band and the aluminum was then produced during surface melting and refreezing by an electron beam scan. The degree of mixing was monitored as a function of scan velocity of the electron beam (related to the solidification velocity) and the power level of the beam (related to the depth of the melt pool).

2

## Task Objective

The objective of this work is to develop guidelines based on kinetic and thermodynamic solidification theory for prediction and control of rapid solidification processes. In particular, segregation effects and rules governing the formation of equilibrium and non-equilibrium phases, including metallic glasses, will be investigated. Areas where significant improvements in alloy properties can be produced by rapid solidification will be emphasized.

## Technical Problem and General Methodology

Rapid solidification techniques make it possible to produce new types of materials having significantly better properties than conventionally processed materials. However, improved predictive techniques and control of rapid solidification processes are needed. The current studies are focussed on the science underlying areas where improved materials can be obtained in order to provide such prediction and control. This work is both theoretical and experimental.

Three major ways in which rapid solidification technology provides improved materials are:

1. Production of alloys with new compositions and phases

2. Production of improved alloy properties by control of microstructures and homogeneity in rapidly solidified alloys

3. Production of improved alloy surfaces by rapid solidification

The general method followed in this work has been to identify critical questions in these three major rapid solidification application areas where solidification theory, when properly developed and checked by experiment, can provide improved understanding of important rapid solidification processes. This understanding then is pursued to provide guidelines that can be used by alloy producers to obtain new improved materials and to select optimum

3

alloy compositions and processing conditions for rapid solidification applications.

Results from work on this contract in each of these areas will now be described in more detail.

Technical Results, Important Findings, Plans and Implications for Future Work

1. Production of Alloys with New Compositions or Phases

Rapid solidification allows the partitionless solidification of alloys to produce extended solid solubility, i.e., production of single phase solidified alloys having compositions in two-phase regions of alloy phase diagrams. Production of uniform alloys in these composition ranges normally is not possible by conventional metal processing techniques. However, such homogeneous alloys would be expected to have properties not obtainable by other means. Furthermore, these alloys might be subsequently heat treated to provide very fine precipitates and, by that means, produce material with especially desirable properties. The conditions necessary for producing such alloys are being investigated in the present work to allow prediction and control of these processes.

During rapid solidification the nucleation and/or growth of a thermodynamically stable phase may be difficult, thus making feasible the production of alloys composed of metastable phases. In current work, liquidus, solidus, and other thermodynamic data for metastable phases have been used for the interpretation and prediction of metastable phases present or possible in rapidly solidified alloys. In this approach, extrapolations of stable phase boundaries as functions of temperature, pressure or composition into regions of metastability can often be constructed directly on the equilibrium phase diagram. The coupling of such metastable phase diagrams with a kinetic analysis can contribute toward effective alloy design and processing during rapid solidification.

4

Experiments are underway to allow predictions from this model to be related to measured rapid solidification results.

A preprint of the paper "Use of Metastable Phase Diagrams in Rapid Solidification" discusses some results of the work in detail and is included as an appendix in this progress report.

In experimental studies, emphasis during this reporting period has been on completing a systematic determination of microstructures obtainable in Ag-Cu alloys over a range of Cu composition starting at 1 wt% Cu, below the $\alpha$-phase solubility limit, and extending up to the eutectic composition, 28.1 wt% Cu. Electron beam surface melting-and-refreezing experiments in which the solidification velocity is closely related to the scan velocity of the electron beam across the surface were used for these measurements. At compositions below the solubility limit, morphological stability theory provides a good description of the critical velocity below which cellular microstructures, such as produced by non-planar solidification interfaces, are found and above which microsegregation-free alloys, such as expected from planar solidification interfaces, are created. Above the solubility limit in the extended solid solubility composition range, cellular or eutectic microstructures give way as the solidification velocity is increased, first to a banded structure containing bands of microsegregation-free alloy and then at still higher solidification velocities to a uniformly micro-segregation-free material. The production of homogeneous (micro-segregation-free) alloys at these higher compositions is related to solute trapping. This process is thermodynamically feasible since the $T_0$ curve on the phase diagram remains at moderately high temperatures at all compositions. Consequently, undercooling below temperatures $T_0$, which is required to produce partitionless solidification, is possible at all compositions.

5

## 2. Production of Improved Alloy Properties by Control of Homogeneity in Rapidly Solidified Alloys

Production of finely segregated microstructures can be important in improving mechanical properties in some applications. In other applications, avoidance of microsegregation in alloys will be required.

In current work, conditions controlling these effects are being investigated by both predictive calculations and experimental measurements. It is found that planar solidification interfaces, which allow avoidance of microsegregation, can be produced by imposing very rapid solidification velocities. Critical velocities for the transition from cellular to planar interfaces have been calculated and in some cases confirmed by experiment. In the cellular regime, cell spacings and resulting segregation effects have been calculated as a function of rapid solidification conditions.

Non-equilibrium effects also may considerably influence some rapid solidification results. Linear perturbation theory has been used to study morphological instability for rapid directional solidification at constant velocity under conditions where there is significant departure from local equilibrium at an initially planar solid-liquid interface. It is found that when the segregation coefficient $k$ depends significantly on the solidification velocity $v$, oscillatory instabilities leading to three-dimensional segregation patterns can be produced. A preprint of the paper "Oscillatory Morphological Instabilities Due to Non-Equilibrium Segregation" which presents these results is included as an appendix in this progress report.

6

## 3. Production of Improved Alloy Surfaces by Rapid Solidification

Alloy surfaces can be appreciably modified by providing local heating from a directed energy source, such as an electron beam or a laser, to melt the surface locally and then creating rapid solidification by removing the energy source, for example, by moving the beam away across the surface. Highly homogeneous material can be produced by this rapid solidification process only if the liquid phase itself is sufficiently homogeneous. In current work, experiments have been carried out to determine more clearly the role of convective mixing in producing such homogeneity and to give an indication of the magnitude of some of the flow velocities. Some of these results are included in a paper "Processing/Microstructure Relationships in Surface Melting" which is included as an appendix in this progress report. That paper also discusses interface morphological stability results and some heat flow considerations. A more detailed discussion of homogenization by electron beam surface melting is presented now as part of this report.

### *Homogenization by Electron Beam Surface Melting*

Highly homogeneous materials can be produced by rapid solidification only if the liquid phase itself is sufficiently homogeneous. For powders produced from atomized liquids or for ribbons produced by processes such as melt spinning, homogeneity of the liquid can usually be attained by holding the melt for a sufficient time, but for surface melting by directed energy sources the time in the liquid phase is usually very short. Therefore rapidly solidified surface melted layers often show significant large scale inhomogeneity if the initial material has a coarse pattern of microsegregation or if a deposited layer is being melted into a substrate for surface alloying.

For a melt pool of radius a moving at a velocity v, the time in the liquid state is $2a/v$, and the typical distance which a solute moves by diffusion during this time is approximately $(2aD/v)^{1/2}$, where D is the solute

7

diffusivity. Typical values in a surface melting experiment would be $a = 5\times10^{-4}$ m, $v = 10^{-1}$ m/s, and $D = 2\times10^{-9}$ m$^2$/s, giving $10^{-2}$ s in the liquid state and a diffusion distance of slightly less than 5 μm, which would be inadequate for homogenization of most conventional microstructures.

It is well known, however, that strong convective flow is normally present in melts made by directed energy heating. This convection can be attributed primarily to the Marangoni effect, i.e., it is driven by the temperature dependence of the liquid surface energy. Because the temperature gradients in the liquid are frequently of the order of $10^6$ K/m, this effect has the potential to drive rapid rates of fluid flow even within the confines of a very small liquid pool. In most surface melting experiments, however, the surface is not sufficiently clean that the surface energy or its temperature dependence can be accurately estimated.

A conspicuous effect which is sometimes present in surface melts and which is usually attributed to fluid flow is the topographic relief which remains on the surface of the melt trail after solidification. Frequently this relief takes the form of a high narrow ridge along the centerline of the melt pass with corresponding depressions along either side. There can also be a net longitudinal transport of material in the melt path, usually in the direction opposite to that of the beam motion. The topographic relief features can attain bizarre extremes if multiple passes are made over the same area. Among the materials which we have studied, these effects seem to reach their extreme in Cu or alloys with high Cu concentration, but to be of relatively little importance in Al and its alloys. In most cases we have found that the topographic effects can be minimized by a proper selection of the beam power level and diameter.

8

Convective flow in the melt is also influenced by the formation of a plasma above the sample surface. In electron beam melting, several effects are seen when the beam current density becomes high enough to ignite the plasma;

1) The fraction of the beam current actually entering the target decreases and becomes extremely "noisy";

2) Transverse ripples and other topography become much more prominent on the surface of the melt path;

3) The melt may start to transform to the deep penetration mode in which the depth is greater than the width.

Thus, although the formation of a plasma is probably accompanied by a more turbulent mixing of the melt with consequent improved homogenization, the formation of undesirable surface relief may negate the usefulness of this mixing mechanism.

To obtain the best possible homogenization by surface melting, it is frequently necessary to precede the final high speed surface melt by a preliminary melt at intermediate speed which serves to reduce the scale of the microstructure in the substrate. For example, many of the Ag-Cu alloys studied in another part of this project were initially homogenized by scanning the entire surface at velocities of approximately 2.5 cm/s. This allows adequate time for convective mixing in the melt but also produces a microstructure which is fine enough to homogenize by liquid diffusion in the subsequent higher speed melts.

Experiments have now been carried out to determine more clearly the role of convective mixing and to give an indication of the magnitude of some of the flow velocities. A fine copper wire was pressed into the surface of a block of pure aluminum and the sample was then heated to 560 °C under vacuum to produce a narrow band (about 1 mm wide) of molten eutectic

9

across the surface of the still solid aluminum. After furnace cooling, this band consisted of coarse primary dendrites in a eutectic matrix. Electron beam melt passes were then made across the surface of the sample in a direction perpendicular to the eutectic band, at several velocities and power levels. Microscopic observations were made of the sample surface and of a section parallel to the original surface but slightly below it.

The shape of the trailing edge of the melt pool is revealed by the ripples which remain behind on the sample surface. Thus it can be seen that as the melt pool crosses the alloyed region and becomes heavily loaded with solute, the trailing edge transforms from a rounded to a more pointed shape. As the solute concentration of the melt pool subsequently diminishes again, the rounded trailing edge reappears.

When the electron beam power is low ($\sim$400 W), so that at the depth of the observed section melting occurs only in the alloyed zone but not in the pure aluminum substrate, one observes a partial melting of the primary dendrites within the alloyed zone. At a beam scan velocity of 0.2 m/s the alloyed zone remains above the eutectic temperature for approximately 5 ms, and the evidence of melting consists of a refinement of the eutectic structure plus a very fine scale mottled appearance in the primary phase particles, especially near their peripheries. The appearance of the mottled region is suggestive of partial melting in a region which has been briefly heated above its solidus temperature, but for a time which was too short to allow the liquid formed in this region to make contact with and mix into the surrounding eutectic liquid. Therefore even if convection is present in the eutectic liquid, there are not sufficient compositional differences in this liquid to leave an indication of its magnitude or direction.

At an electron beam scan velocity of $2 \times 10^{-2}$ m/s, melting at the same

10

power resulted in more extensive dissolution of the primary particles and mixing into the surrounding liquid. Aluminum-rich material can be seen streaming away from the dissolving primary particles into the eutectic liquid. These streams can be seen to have carried material for at least 200 $\mu$m. during the approximately $5 \times 10^{-2}$ s that the material was molten, which implies that the flow velocity was at least $4 \times 10^{-3}$ m/s, but possibly much larger because one cannot tell if the streams have merely dissipated into the melt beyond 200 $\mu$m.

At higher power levels the fluid flow effects are much more conspicuous. At 700 W, with the same velocities used above, the pure aluminum as well as the primary particles in the alloyed zone were melted at the depth of the metallographic section. It was found that copper had been transported a considerable distance upstream in the weld pass, indicating that the copper became dispersed throughout the melt pool very rapidly after the eutectic band was encountered. At a scan speed of 0.2 m/s, the mixing in the melt zone appears incomplete whereas at a scan speed of $2 \times 10^{-2}$ m/s the melt zone was more thoroughly homogenized. The distance of upstream motion at the more rapid scan speed implies a fluid flow velocity of at least 0.2 m/s.

Metallographic sections of 2024 aluminum alloys melted at a range of velocities show evidence of residual liquid inhomogeniety at high melt velocities but not at velocities of $5 \times 10^{-2}$ m/s or less. This implies that a melt time of approximately 20 ms is sufficient to effectively homogenize the melt. However, in stationary melts of the same alloy, evidence of some inhomogeniety is present even at times as long as 200 ms. These observations suggest that mixing is significantly slower in stationary melts than in moving melts.

11

Measurements to date have thus indicated that in most cases the liquid in melt zones approximately $10^{-3}$ m in diameter is effectively homogenized at scan velocities of $2 - 5\times10^{-2}$ m/s or less. Convective fluid flow, which may involve velocities of 0.2 m/s or greater, is an essential part of the homogenization process. The convective mixing appears to be more effective in moving melts than in stationary melts, and excessive convective flow can lead to the development of undesirable surface topographies.

# USE OF METASTABLE PHASE DIAGRAMS IN RAPID SOLIDIFICATION

J. H. PEREPEZKO, Department of Metallurgical and Mineral Engineering,
University of Wisconsin, Madison, WI 53706 and W. J. BOETTINGER,
Metallurgy Division, National Bureau of Standards, Washington, DC 20234

## ABSTRACT

During rapid solidification, the nucleation and/or
growth of a thermodynamically stable phase may be difficult.
In this case the liquidus, solidus or other thermodynamic
data for a metastable phase are important for the inter-
pretation and prediction of the phases present in rapidly
solidified materials. In this paper various techniques
are described to obtain information about metastable
equilibrium from measured stable equilibrium data. Extra-
polations of phase boundaries as functions of temperature,
pressure or composition (including a new component) into
regions of metastability can often be constructed directly
on the equilibrium diagram. These constructions can be
performed more quantitatively with analytical methods
using thermodynamic modelling of the free energy functions
consistent with measured data. A number of examples are
considered including a discussion of metastable liquid
miscibility gaps, metastable eutectic and peritectic
reactions, pressure diagrams and metastability in ternary
alloys to indicate the possible product phase selection.
A coupling of metastable phase diagrams with a solidifica-
tion kinetics analysis can contribute towards effective
alloy design and processing during rapid solidification.

## INTRODUCTION

In many materials processing treatments such as solidification, the
application of phase diagram information has played a vital role. During conven-
tional solidification processing phase diagrams are used to predict product
phases and to analyze solute segregation distributions based upon a partition
coefficient obtained from the liquidus and solidus phase boundaries. In
practice, due to diffusion limitations and fluid flow, the application of phase
diagram information is restricted to local conditions at the solidification
interface. However, within these limitations the combination of diffusion and
heat flow analysis with phase diagram information has allowed the treatment of
a wide range of solidification processes [1].

Within the domain of Rapid Solidification Processing (RSP), phase diagrams
should also have an important role in the interpretation of possible product
phases and solidification paths. Equilibrium phase diagrams are most useful in
predicting the occurrence of stable phase products. However, during rapid solid-
ification, the nucleation and/or growth of a thermodynamically stable phase from
the liquid may be difficult depending on the details of the respective kinetics.
In this case the liquidus, solidus, partition coefficient or other thermodynamic
data for a metastable phase are important. A schematic representation of the
role of nucleation kinetics and growth kinetics for phase selection as of
function of processing conditions is shown in Fig. 1. The thermodynamic rela-
tions for a liquid, stable phase $\alpha$ and a metastable phase $\beta$ are shown in Fig. 1a.

The given conditions apply strictly only to a pure component or inter-metallic compound, but in an approximate sense could apply to eutectics, for example. In Figs. 1b and 1c a possible pair of functions are depicted to illustrate the role of kinetics in phase selection. For the nucleation of α or β from the liquid the dominant product phase is determined to a large extent by the lowest value of the activation energy barrier for nucleation, $\Delta G^*$, which is shown as a function of temperature in Fig. 1b. In this illustration, $\Delta G^*$ is given [2] for a spherical cap nucleus by

$$\Delta G^* = \frac{16\pi\sigma^3 T_m^2 f(\theta)}{3(\Delta H \Delta T)^2} \tag{1}$$

where $\sigma$ is the liquid solid surface energy, $T_m$ is the melting point, $T_m^\alpha$ or $T_m^\beta$, $\Delta H$ is the latent heat, $\Delta T$ is the undercooling below the melting point and $f(\theta)$ is a factor related to the contact between the nucleus and a catalytic surface. Detectable nucleation is normally associated with values of $\Delta G^*$ less than about $60kT$ [3] where k is the Boltzmann constant. For the $\Delta G^*$ relationships presented in Fig. 1b nucleation of α dominates at low undercoolings below the stable melting point, whereas at lower temperatures nucleation of β can dominate. There are a number of examples of a nucleation controlled transition in phase selection with increasing undercooling including the formation of metastable allotropic phases in pure Ga [4] and Bi [5] and metastable alloy phases [5,6]. This behavior is controlled mainly by the terms $[\sigma^3 f(\theta)]$ and can occur even though the bulk thermodynamic diving force per unit volume ($\Delta H \Delta T/T_m$) is usually greater for the stable phase.

The growth of a stable phase can also be difficult. Following nucleation of two phases from the melt, one phase may grow so much more quickly that it will dominate the microstructure of an RSP alloy. A simple example is illustrated in Fig. 1c which shows schematically the growth rate of the α and β phases from the liquid as a function of interface temperature. For modest excursions below the melting point the growth rate, V, may be related [2,3,7] to the undercooling approximately by

$$V = \frac{V_o \Delta S_m \Delta T}{kT} \tag{2}$$

where $V_o$ is a term related to transport in the liquid and interfacial characteristics (i.e. site density), and $\Delta S_m$ is the entropy of fusion. At low undercooling below $T_m^\alpha$, α phase grows most rapidly. At high undercooling, however, a metastable β phase could grow more rapidly. This could happen, for example, if α phase grows with an atomistically smooth interface, and consequentially small value for $V_o$. Similar kinds of growth competition between phases can depend on the amount of solute partitioning required for the growth of various competing phases or even on the kinetic competition with various eutectics [8]. The competition between the α-Al + Al$_3$Fe eutectic with the α-Al + Al$_6$Fe eutectic is an excellent example of such growth [9,10]. Here the relatively sluggish kinetics of the growth of the α-Al + Al$_3$Fe eutectic is caused by branching difficulties [8]. At growth rates greater than 1 mm/sec., the metastable eutectic involving α-Al + Al$_6$Fe dominates the microstructure.

The nucleation and growth difficulties of some stable phases that can occur in RSP, naturally lead to an expanded utilization of phase diagrams; in particular these constraints require a close examination of the metastable equilibrium features of phase diagrams. At the onset it should be emphasized that a metastable equilibrium is a true reversible equilibrium [11]. It is also useful to note that with stable equilibrium there is a certainty of phase prediction. With metastable equilibrium this certainty of prediction becomes a choice of product phases depending on the particular constraints imposed on the system
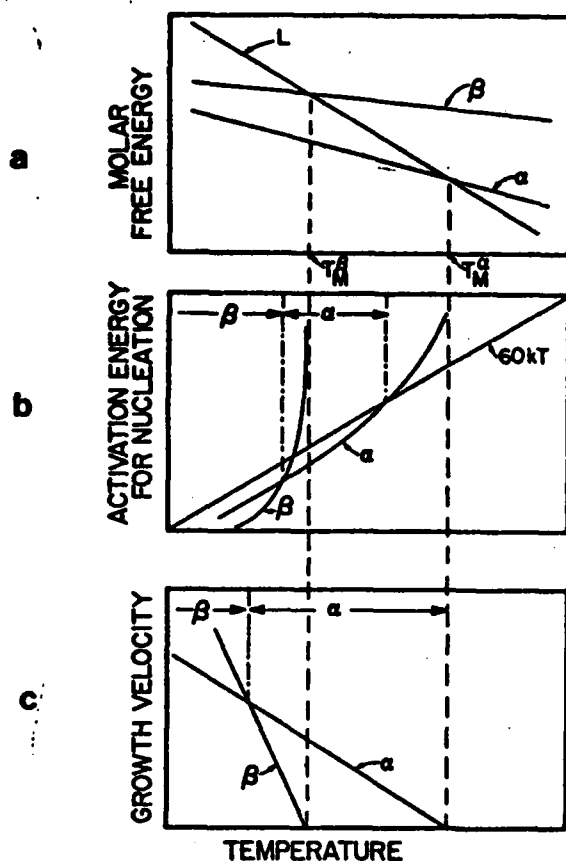
Fig. 1. Schematic representation of the operation of competitive
phase selection kinetics which favors the formation of a
metastable phase β from the liquid L at low temperature
in spite of a) the thermodynamic stability of α. b) Shows
the temperature range for faster nucleation of β phase
while c) shows the temperature range for faster growth of
the β phase.

and the controlling phase selection kinetics. Indeed, current practice in the
processing of important materials such as steels and cast irons routinely
involves the consideration of metastable equilibrium conditions. The advent of
RSP promises to make similar considerations commonplace for a larger class of
materials.

In the present paper a number of useful graphical methods are described
which allow metastable equilibrium phase boundaries to be inferred from existing
equilibrium phase boundaries. In some cases a few of these methods are already
in use. However, during RSP, large excursions into metastable regions are
possible so that some precautionary measures are in order to indicate the
limitations of phase boundary extrapolations. Other features that can be includ-
ed in a metastable phase diagram involve constructions that are not derived
from existing equilibrium boundaries, but serve as useful guidelines for the
thermodynamic bounds on the formation of metastable phases. While many of the
graphical methods can give useful information as a first order approximation,
these constructions can be performed more quantitatively with analytical
representations of the free energy functions. Certainly, as phase diagram models
become more accurate and sensitive, it is likely that metastable data may be
routinely reported together with equilibrium data.

To determine processing treatments required for the formation of novel microstructures [12], it is necessary to have some information on the possible existence range of a given phase in the metastable domain. A first level of such information is the metastable melting temperature of the phase. Based upon this temperature, a measure of the minimum undercooling needed prior to nucleation of the metastable phase can be estimated and competing solidification reactions can be identified.

Some of the simple graphical methods of metastable phase liquidus and solidus temperature determination are illustrated in Fig. 2 for a β phase normally involved in a peritectic reaction and can be applied to other phase reactions such as the metatectic reaction [13]. The melting temperature for the β phase of component A is given by the intersection of the extrapolated liquidus and solidus for β. In Fig. 2a and b the intersection yields the highest temperature at which β can exist in the absence of α phase as discussed also by Hillert [14]. While this method appears quite straightforward, it can not be applied without caution. For example, the situation where the intersection of the β liquidus and solidus occurs before the pure component composition is illustrated in Fig. 2c. In this case a congruent point maximum is required. The accuracy of this method is clearly dependent on the extent of composition range involved in the phase boundary extrapolation and on the curvatures of the liquidus and solidus.

For the pure component $T_m^\beta$ lies between $T_m^\alpha$ and the allotropic transition temperature, $T_{\alpha/\beta}$, and can be calculated from the equilibrium transformation temperatures and transformation entropies. For example, when specific heat corrections are neglected, the value of $T_m^\beta$ is given as

$$T_m^\beta = \frac{[\Delta S_{\alpha/\beta} \, T_{\alpha/\beta} + \Delta S_m^\alpha \, T_m^\alpha]}{\Delta S_{\alpha/\beta} + \Delta S_m^\alpha} \qquad (3)$$

where $\Delta S_{\alpha/\beta}$ is the entropy change for the allotropic transition and $\Delta S_m^\alpha$ is the entropy of melting for α phase. A partial list of melting temperatures for allotropic phases determined by thermodynamic calculation based on data compiled by Hultgren et. al [15] and extrapolation of phase diagram boundaries [16,17] is given in Tables 1 and 2 respectively for a number of metals of interest in RSP.

The comparison of melting points determined by phase boundary extrapolation and by thermodynamic calculation indicates that when the equilibrium phase boundaries are well-defined, the results of extrapolation and calculation agree to within about 10°C. In addition, the results presented in Table 1 give the minimum undercooling, $\Delta T$, below the stable melting point, $T_m^{Eq}$ for the formation of an allotropic phase during RSP. It is interesting to note that for Fe, Mn and Be potential metastable phases require only relatively modest undercooling.

During RSP which involves alloy liquid undercooling ranges that can extend up to about $0.3T_m$ the results listed in Table 1 and Table 2 also reveal the potential for metastable phase formation in a number of alloy systems; especially systems based on Fe, Mn and Be. A very clear demonstration of this potential is provided by the thorough study reported by Cech [18] on the solidification of undercooled Fe-Ni alloys. This system has a phase diagram similar to Fig. 2a with α as a BCC structure and β as an FCC structure. For alloy compositions ranging up to 32 w/o Ni which lie outside of the equilibrium BCC phase field Cech documented that a BCC structure nucleates from undercooled liquid droplets. While this result seems impossible in terms of the equilibrium phase diagram, an interpretation is possible in terms of the
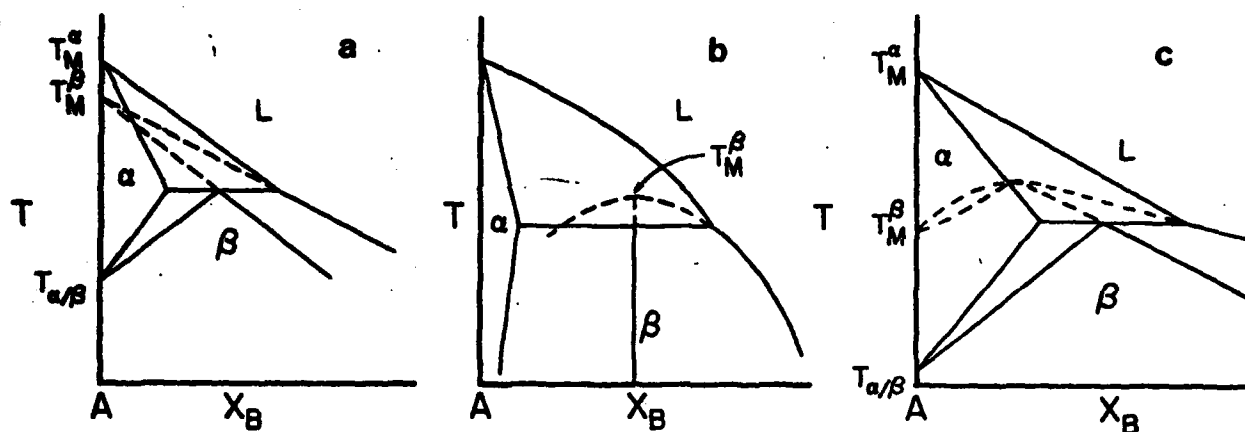
16

Fig. 2. Metastable extension (dashed) of β phase liquidus and solidus curves in the absence of α phase. a) Indicates a metastable melting point $T_M^\beta$ of pure A. b) Indicates the melting point of β phase as a line compound and c) indicates an azeotrope or maximum in the metastable extension.

TABLE I
Calculated Melting Points of Allotropic Phases

|  | $T'_m$ (°C) | $\Delta T = [T_m^{Eq} - T'_m]$ (°C) |
|---|---|---|
| Fe [L→γ(FCC)] | 1531 | 5 |
| Mn [L→γ(FCC)] | 1228 | 16 |
| Mn [L→β ] | 1208 | 36 |
| Be [L→α(HCP)] | 1282 | 5 |
| Ti [L→α(HCP)] | 1518 | 152 |
| Zr [L→α(HCP)] | 1550 | 302 |

TABLE 2
Melting Points of Allotropic Phases from Phase Diagram Boundary Extrapolation

|  | Alloy System | $T'_m$ (°C) |
|---|---|---|
| Fe [L→γ(FCC)] | Fe-C | 1530 |
|  | Fe-Ni | 1527 |
|  | Fe-Co | 1521 |
| Mn [L→γ(FCC)] | Mn-Ni | 1224 |
|  | Mn-Ge | 1217 |
| Mn [L→β ] | Mn-Si | 1225 |

17

metastable phase diagram since the solidification of the undercooled liquid can occur within the metastable L+α two-phase field generated by extending the α phase liquidus and solidus boundaries to higher solute content. The same type of phase boundary extrapolation can be used to understand the report [19] of a significant extension of the narrow stable γ phase field in Sn-Cd alloys following rapid liquid quenching. Similarly, the metastable extension illustrated in Fig. 2b shows clearly that during solidification of alloys near a peritectic reaction the product β phase can exist and grow above the peritectic isotherm [14] as observed in the Sn-Cd [20] and Pb-Bi [21] systems. It should be noted that the details of the competitive kinetics that favor the selection of a given metastable structure over an equilibrium structure require additional analysis. At the same time, however, the realization of metastable structure possibilities can serve to demystify many RSP results.

In addition to methods based upon graphical extrapolations of phase boundaries involved with peritectic reactions, a similar approach may be applied to eutectic systems as shown in Fig. 3. If the crystal structures of the α,β and γ phases are different, then the liquidus and solidus boundaries for each of the alloy phases can be extended to the pure component sides of the phase diagram and a rough estimate can be obtained for the melting temperature of the pure phases. The construction is demonstrated in Fig. 3a for an alloy system displaying peritectic and eutectic reactions and so illustrates the approach followed in model calculations of phase diagrams [22]. While the eutectic extrapolation is similar to the peritectic extrapolation in which the metastable melting temperature of the pure component is given by the intersection of the extended liquidus and solidus, the uncertainty can be greater for the eutectic case due to the usually larger composition range of extrapolation. Furthermore, a congruent point giving a metastable liquidus and solidus minimum may develop before extrapolation to the pure component composition. As a result, extrapolations based upon liquidus and solidus boundaries for eutectics should be supplemented by thermodynamic model calculations for the most useful determinations.
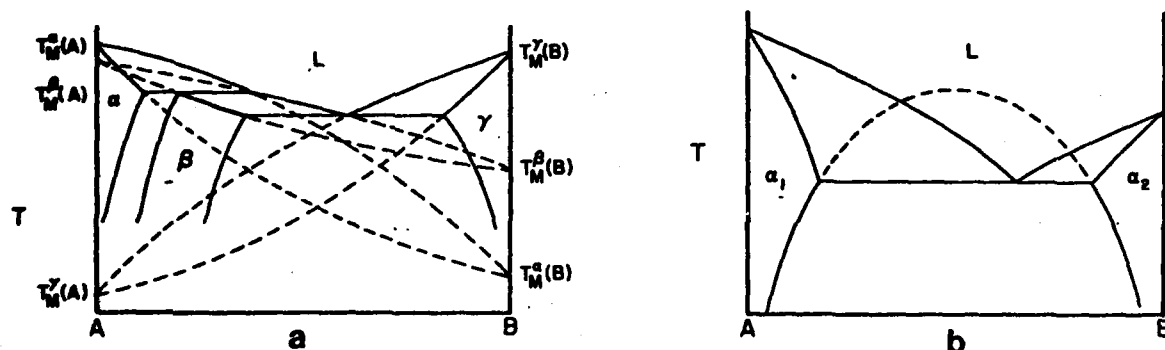


Fig. 3. a) The stable phase diagram contains a peritectic and eutectic between phases of different crystal structure. The pure component melting temperatures of three structures are shown. In the absence of α and γ, for example, β phase could form at any composition. b) Metastable extension (dashed) of the solvus curves above the eutectic temperature to a critical point when the crystal structures of the two solid phases $\alpha_1$ and $\alpha_2$ are the same.

An important feature of RSP is illustrated by the constructions given in Fig. 3a. If an alloy is cooled sufficiently so that the liquid is within the metastable two-phase field, such as L + α, it is possible to form α over a much wider composition range as a single phase product than predicted by the equilibrium diagram. Of course, the stability of such a single

phase depends on the diffusional kinetics of decomposition and other thermo-
dynamic conditions such as the presence of a spinodal in the solid state
(not present for the conditions in Fig. 3a). For both peritectic and eutectic
diagrams involving a miscibility gap between adjoining phases of the same
crystal structure, it is often possible to judge the relative location of
the gap by extending the solvus phase boundaries as indicated in Fig. 3b. From
the critical temperature of the miscibility gap, the spinodal curve may be
calculated to identify the stability limit of a solid solution. Again the extent
of extrapolation usually indicates a need for model calculations to define the
correct boundary positions and may also require a consideration of coherency
strain energy [23] to establish the actual stability limit of a solid solution
to a fine scale decomposition.

Many phase diagrams display multiple peritectic and eutectic reactions.
The extrapolation constructions applied to these reactions reveal an equally
large number of metastable phase reactions and some interesting implications
for RSP treatments. For example, with a phase diagram consisting of a series
of adjacent eutectic reactions, the extension of the equilibrium liquidus
phase boundaries to an intersection will yield the location of each metastable
eutectic point. From the phase boundary relationships indicated in Fig. 4a,
it is apparent that the composition of the metastable eutectic points need not
be close to the equilibrium eutectic points. In fact, as reported in a number
of alloy systems including Fe–Ge and Cd–Sb [16] the metastable eutectic point
can be close to the composition range of an equilibrium intermediate phase.
For the interpretation of eutectic structures resulting from RSP treatment the
realization of the pertinent eutectic reaction is clearly necessary. Further,
it is a common rule that the composition regions of relatively easy glass forma-
tion tend to lie near deep eutectics. The presence of intermediate compound
phases has also been reported as a possible factor in easy glass formation [24].
Many intermediate compound phases have complex crystal structures and can
exhibit relatively difficult crystallization from the melt. Since glass forma-
tion requires deep excursions into the metastable regions of the phase diagram,
it seems most appropriate to relate any possible phase diagram features involved
with glass formation to the full possibilities of the metastable phase
diagram where equilibrium compound phases may be absent and eutectic points
displaced in composition and temperature. Indeed, the glass formation charac-
teristics in systems such as Ni–Nb and Cu–Zr may be examples of this behavior.

For an alloy sytem containing multiple adjacent peritectic reactions both
metastable peritectic and eutectic reactions may be generated by the extension
of the equilibrium liquidus phase boundaries. The construction is illustrated
by the schematic diagram in Fig. 4b and 4c where the stability range of some of
the intermediate phases has also been extended upward in temperature. In the
absence of the intermediate β phase, the extrapolations in Fig. 4b indicate the
development of a metastable peritectic involving the α and γ phases. Alternately
the extrapolations of the α-liquidus and γ-liquidus boundaries in Fig. 4c may
lead to the development of a metastable eutectic reaction (L→α + γ). In this
case the course of the solidification path and microstructure development
indicated by the equilibrium phase diagram will be altered during RSP. As in the
extrapolation methods for single peritectic and eutectic reactions described pre-
viously, the phase boundary extensions for multiple reactions must be performed
with caution. Also it is possible that new metastable intermediate phases may
form as in the Al–Fe [9] system and alter the peritectic and eutectic reactions
relevant to the interpretation of an RSP microstructure.

Another metastable equilibrium feature that can modify the course of phase
boundary extrapolations and the development of microstructure is the appearance
of a miscibility gap in the undercooled liquid. Often the tendency for a liquid
or solid state demixing reaction can be judged by the appearance of the phase
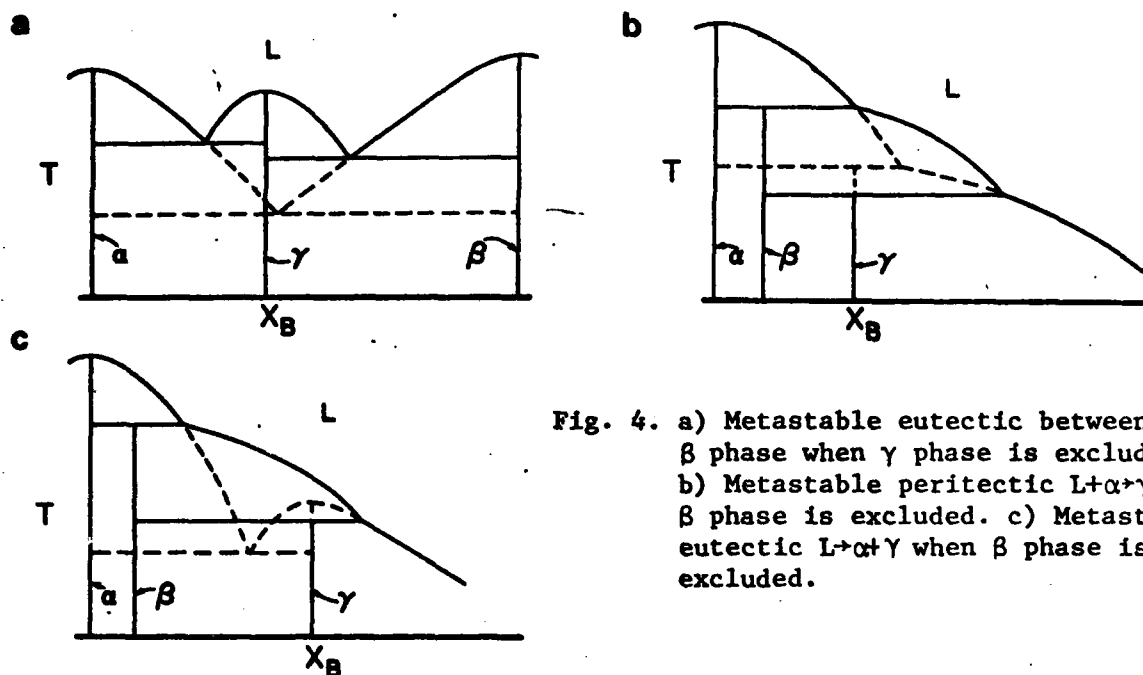boundary; in particular, the slope and curvature of the liquidus or solidus.

**Fig. 4.** a) Metastable eutectic between $\alpha$ and $\beta$ phase when $\gamma$ phase is excluded. b) Metastable peritectic L+$\alpha$→$\gamma$ when $\beta$ phase is excluded. c) Metastable eutectic L→$\alpha$+$\gamma$ when $\beta$ phase is excluded.

The occurrence of a "submerged" liquid miscibility gap is illustrated in Fig. 5 for an equilibrium eutectic system with limited solid solubility and a positive heat of mixing. The thermodynamic conditions favorable to a liquid phase separation may be examined in terms of the relation for the slope of the liquidus for binary alloys which can be given by the Gibbs-Konovalov equation [25] as

$$\frac{dT_L}{dX_A} = \frac{X_A^L \, T_L \, G_{XX}^L}{\Delta H_{FP}^B} \tag{4}$$

where $T_L$ is the liquidus temperature, $X_A^L$ is the mole fraction of A in the liquid, $G^L$ is the Gibbs free energy for the liquid, $\Delta H_{FP}^B$ is the molar enthalpy change for the formation of a minute amount of solid from the alloy liquid, and $G_{XX}^L$ is the second compositional derivative of the Gibbs free energy for the liquid. For a regular solution [26], $G_{XX}^L$ can be expressed in terms of the interaction parameter, $\Omega$, by

$$G_{XX}^L = \frac{RT}{X_A(1-X_A)} - 2\,\Omega \tag{5}$$

where R is the gas constant and $\Omega = 2RT_c$ with $T_c$ representing the consolute temperature of the miscibility gap. The value for $\Delta H_{FP}^B$ is obtained from the relation

$$\Delta H_{FP}^B = H_S^{\ B} - (H_L^B - X_A \frac{dH_L^B}{dX_A}) \tag{6}$$

which reduces in the regular solution model to
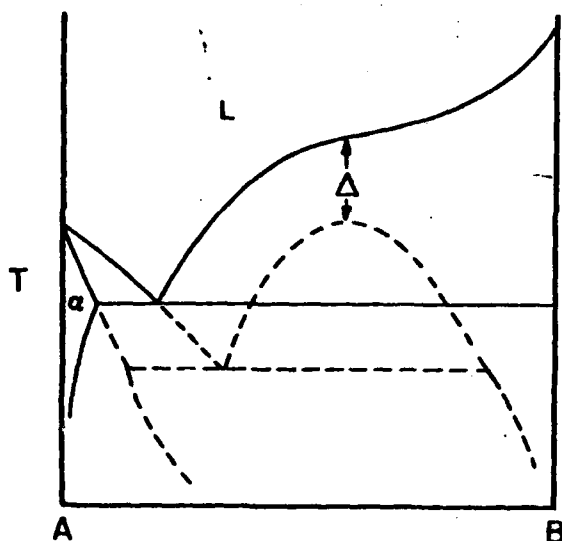
$$\Delta H_{FP}^B = -L_B - X_A^{\ 2}\,\Omega \tag{7}$$

20

Fig. 5. Metastable liquid miscibility gap and the associated monotectic reaction (dashed) when solid B phase is excluded, The difference, $\Delta$, between the stable liquidus and the miscibility gap critical point is proportional to the slope of the stable liquidus above the critical point.

where $L_B = H_L^B - H_S^B$ is the heat of fusion for component B. For the purpose of illustration the combination of equations (4), (5) and (7) yields an expression for $\Delta = T_L - T_C$ which for the equiatomic composition is

$$\Delta = \frac{L_B + 1/2\ RT_C}{2RT_L} \left[ \frac{-dT_L}{dX_A} \right]_{X_A = 0.5} \tag{8}$$

Although the expression for $\Delta$ may be given in an alternate form in terms of other parameters [27], equation (8) indicates the relation between the magnitude of $\Delta$ and the liquidus slope. When the liquidus is horizontal, the consolute point touches the liquidus and $\Delta$ is zero. Increasing values for the liquidus slope depression correspond to greater values of $\Delta$. However, it should not be inferred that a "submerged" miscibility gap exists below all flattened liquidus phase boundaries [25].

Several examples of metastable miscibility gaps in metallic alloys have been reported for systems such as Fe-Cu and Co-Cu at $\Delta$ values of 20°C and 90°C respectively [28]. Also, for the Cu-Nb system microstructural features in chill cast alloys [29] suggest the presence of a metastable miscibility gap at modest undercooling. In fact the miscibility gap appears to become thermodynamically stable upon addition of oxygen. At the high undercooling values expected during RSP the consideration of liquid phase separation is likely to be more common. Since it is difficult to suppress liquid separation even at the high cooling rates characteristic of RSP, it is necessary to incorporate the influence of a possible liquid phase separation reaction on the solidification path and microstructure. In fact, it is probable that phase separation reactions can influence the course of devitrification of amorphous alloys during heating [30].

TERNARY ALLOYS

Practical alloys only rarely contain two components and an examination of various metastable equilibrium features of ternary alloys is instructive. In ternary alloys, phase boundaries are typically surfaces in three dimensional temperature-composition diagrams. Metastable extensions are only geometrically more complicated than those already described. Of interest in RSP is the ternary liquidus surface to which the discussion will be restricted. The total liquidus surface, for example, consists of a series of curved surfaces of primary crystallization of the various phases. Two surfaces can intersect and form
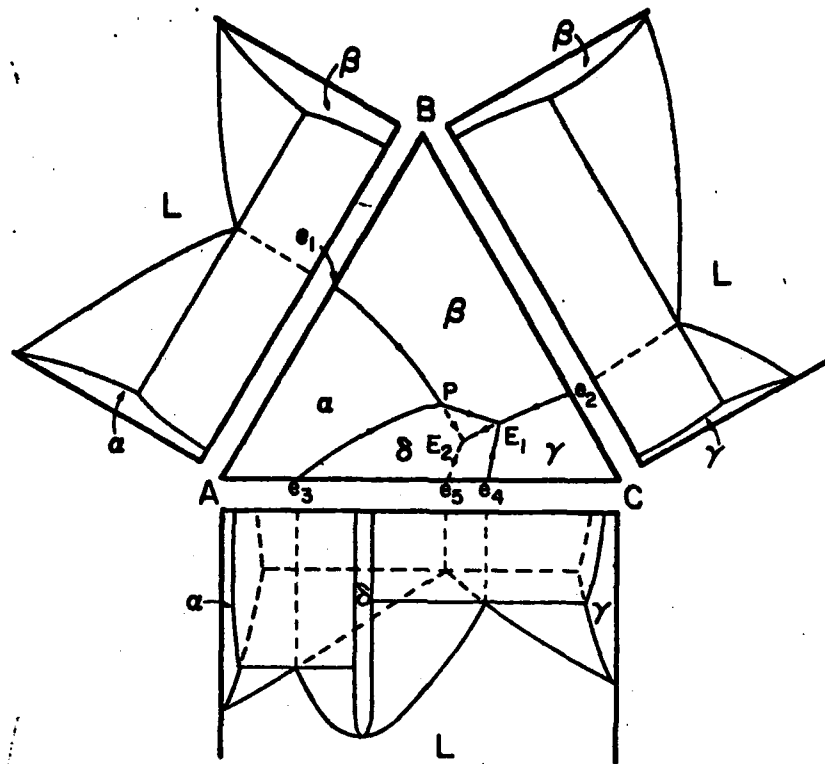
Fig. 6. Metastable ternary liquidus surface when the δ phase is excluded.
The metastable binary eutectic L→α+γ ($e_5$) gives rise to a
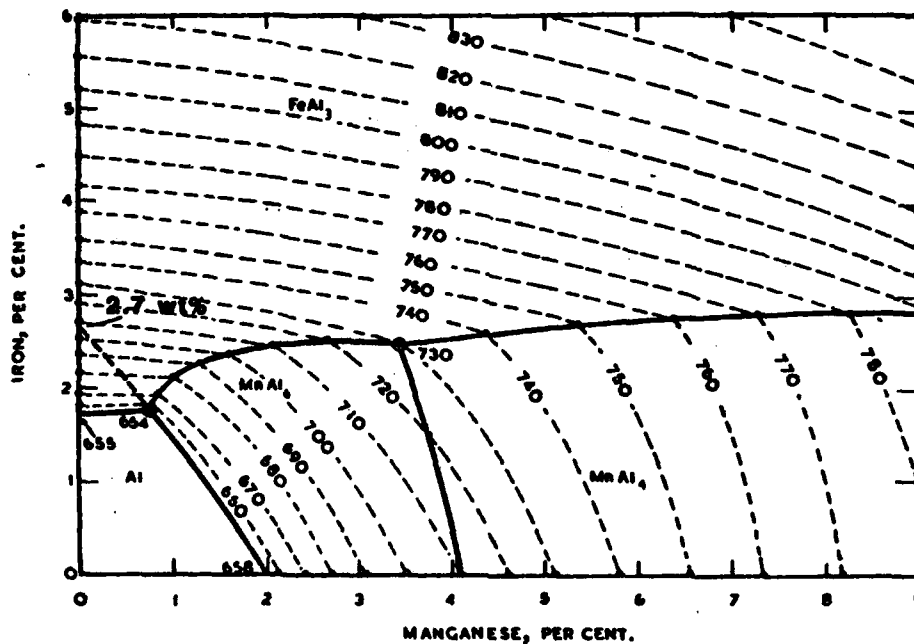metastable ternary eutectic L→α+β+γ ($E_2$).



Fig. 7. Liquidus surface of the Al-rich corner of the Al-Fe-Mn system [31].
If the phase Fe₃Al does not form, the eutectic valley,
L→α-Al+(Mn,Fe)Al₆, extends to the Al-Fe binary (dashed line).

22

eutectic valleys or peritectic lines where three phases coexist (eutectic or peritectic) or three surfaces can intersect at a point where four phases can coexist (eutectic or peritectic). Figure 6 shows a schematic liquidus surface containing five stable eutectic valleys, a ternary peritectic $L + \alpha \to \beta + \delta$ (point P) and a ternary eutectic $L \to \beta + \gamma + \delta$ (point $E_1$). If it is difficult to nucleate or grow $\delta$ phase, various metastable features of the diagram become important. These metastable features are shown as dashed lines. In the binary diagram between components A and C, elimination of the $\delta$ phase leads to a metastable eutectic at point $e_5$. In the ternary, the liquidus surface and the eutectic valleys involving $\delta$ phase are eliminated as well as the invariant points P and $E_1$. The eutectic valleys, $L \to \alpha + \beta$ and $L \to \beta + \gamma$ will extend beyond points P and $E_1$ respectively until their intersection at point $E_2$. Additionally, the metastable eutectic valley $L \to \alpha + \gamma$ must extend into the ternary from $e_5$ and also pass through point $E_2$. Point $E_2$ is a metastable ternary eutectic $L \to \alpha + \beta + \gamma$ at a temperature below the stable ternary eutectic $L \to \beta + \gamma + \delta$ at point $E_1$. Such metastable eutectics could form the basis for easy glass forming composition ranges that are not usually considered.

The extension of liquidus surfaces beyond lines of intersection with other liquidus surfaces when the associated solid phase is difficult to nucleate or grow leads to the appearance of phases at compositions not normally expected under conditions of stable equilibrium. An example of interest in RSP are alloys in the Al-Fe-X system where X is Mn or Ni. Figure 7 shows the ternary liquidus surface of Al-Fe-Mn [31]. The phase $Al_6(Mn,Fe)$ has considerable equilibrium solubility for Fe permitting substitution of more than half of the Mn atoms with Fe. In fact, the phase $Al_6Fe$ is commonly known to occur in binary Al-Fe alloys solidified at only modest rates as the $\alpha$-Al + $Al_6Fe$ eutectic. An estimate of the temperature and liquid composition for this metastable eutectic can be made by elimination of the $Al_3Fe$ liquidus surface and permitting the continuation of the $L \to \alpha$-Al + $Al_6(Mn,Fe)$ eutectic valley to the Al-Fe binary. This extrapolation, shown in Fig. 7, yields a temperature of 653°C and 2.7 w/oFe for the $\alpha$-Al + $Al_6Fe$ metastable eutectic. The stable eutectic of Al with $Al_3Fe$ is 655°C and 1.8 w/oFe. This metastable eutectic temperature has been measured in droplet solidification experiments to be 649°C [32]. Clearly the small difference between the stable and metastable eutectic temperatures is one reason for the ease at which $Al_3Fe$ is replaced by $Al_6Fe$ in eutectics with Al by slight undercooling prior to solidification or growth at slightly elevated rates (>1mm/s) [9,10].

Another phase more recently found during RSP in the Al-Fe binary system is $Al_9Fe_2$ [33]. If the binary is considered as part of the ternary Al-Fe-Ni system, a ternary phase $Al_9(Fe,Ni)_2$, isomorphous with $Al_9Fe_2$, is found in Fig. 8 [31]. Extension of the $L \to \alpha$-Al + $Al_9(Fe,Ni)_2$ eutectic valley to lower Ni content suggests a $L \to \alpha$-Al + $Al_9Fe_2$ eutectic in binary Al-Fe at $\sim$ 3.3 w/o Fe. The metastable extension of the eutectic valley is the intersection of the metastable liquidus surfaces for $\alpha$-Al and $Al_9(Fe,Ni)_2$. Hence the temperature of this metastable eutectic in binary Al-Fe must be given by the metastable $\alpha$-liquidus curve in the binary at 3.3 w/o Fe. This temperature is estimated as 650°C using an $\alpha$-liquidus slope of 3°C per w/o. Consequently the metastable eutectic valley most likely contains a temperature maximum in the ternary. The observation that $Al_9Fe_2$ is only formed at solidification velocities higher than those required for $Al_6Fe$, is consistent with the prediction of a lower eutectic temperature (650°C compared to 653°C) for $\alpha$-Al with $Al_9Fe$ compared to $Al_6Fe$.

The extension of the $L \to \alpha$-Al + $Al_9(Fe,Ni)_2$ eutectic to the Al-Ni binary diagram reveals a metastable eutectic $L \to \alpha$-Al + $Al_9Ni_2$ at 8.6 w/o Ni and 633°C if the formation of the $Al_3Ni$ phase can be suppressed. A metastable phase has been reported in Al-Ni alloys [34,35] in the composition range of this proposed metastable eutectic, however the reported crystal structure is not isomorphous with $Al_9(Fe,Ni)_2$. Again it should be noted that the detailed
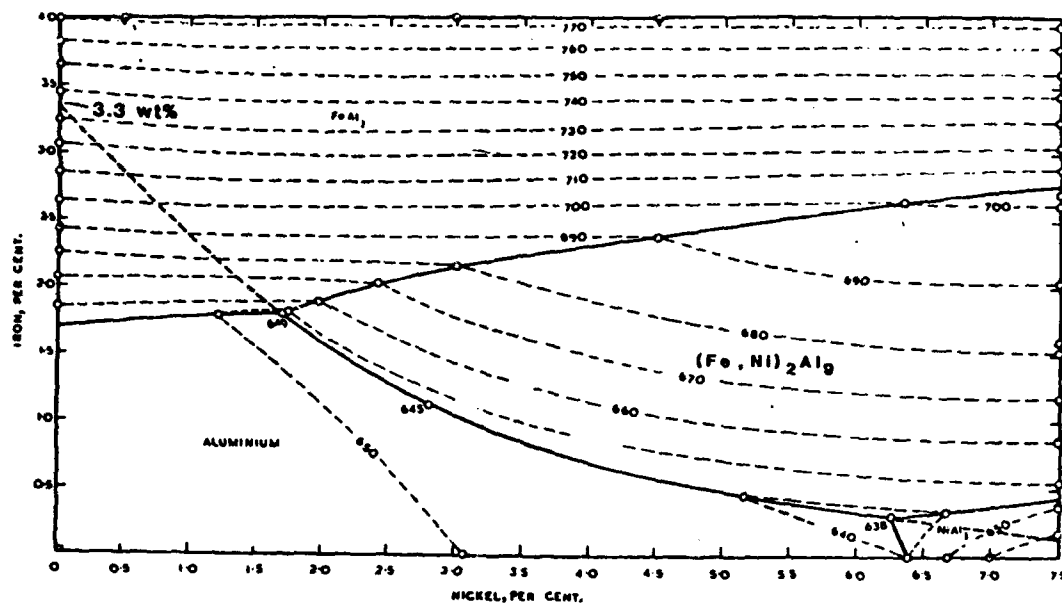
23

Fig. 8. Liquidus surface of the Al-rich corner of the Al-Fe-Ni system [31].
If the phase Fe₃Al does not form, the eutectic valley
L→α-Al (Fe,Ni)₂Al₉, extends to the Al-Fe binary (dashed line).
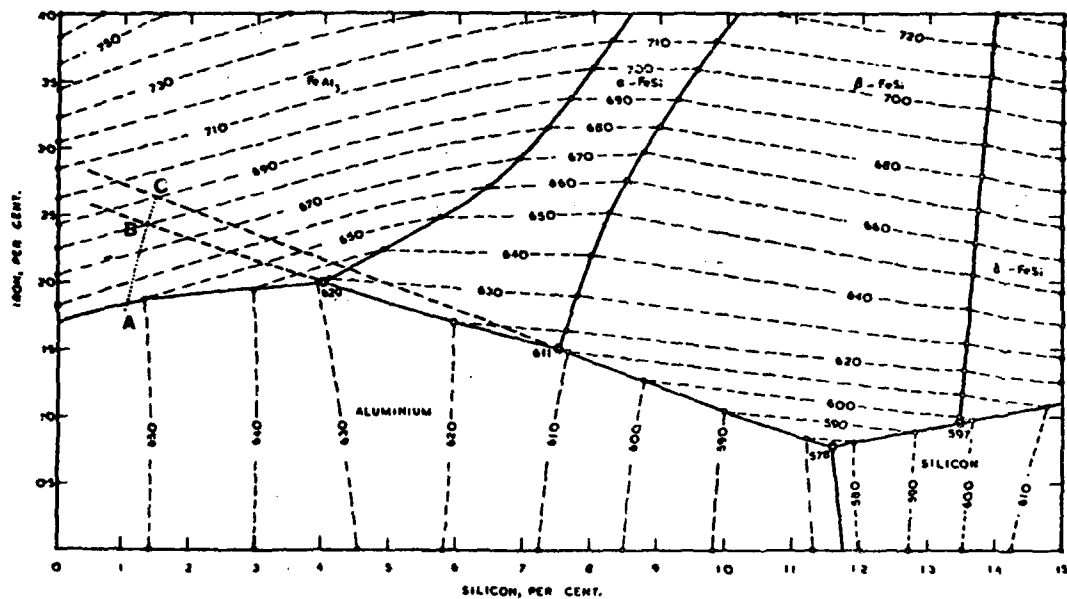


Fig. 9. Liquidus surface of the Al-rich corner of the Al-Fe-Si system [31].
If the phase Fe₃Al does not form, the eutectic valley, L→α-Al+α-FeSi,
extends toward B and the Al-Fe binary.  In the absence of both Fe₃Al
and α-FeSi, the eutectic valley L→α-Al+β-FeSi extends toward C and
the Al-Fe binary.  The solidification path for an alloy of composi-
tion A during formation of primary α-Al would follow the line AB
before the formation of α-FeSi in the first case and AC before the
formation of β-FeSi in the second case.

24

values of the metastable eutectics are intended only to serve as estimates. Computer modelling of the free energy functions consistent with measured phase diagram information should permit more accurate extrapolations in the future.

A common occurrence in RSP multicomponent alloys is the elimination of some of the intermetallic compounds which normally occur in conventionally cast alloys. A striking example is found in an Al-1.8 w/o Fe-1.1 w/o Si alloy solidified by the twin-roll strip casting (Hunter) process [36]. This process produces 7 mm thick sheet at 1.5 cm/s. In conventionally cast direct chill (D.C.) ingots, the microstructure consists of α-Al dendrites and interdendritic α-FeSi ($Al_{12}Fe_3Si_2$). Alloys cast by the Hunter process consists of α-Al and β-FeSi ($Al_9Fe_2Si_2$). The "solidification path", which is the composition of the interdendritic liquid phase during solidification of α-Al can be estimated crudely using the Scheil equation [1] independently for the two components Fe and Si with equilibrium partition coefficients of 0.02 and 0.13 respectively. This calculated path is shown on the aluminum-rich corner of the Al-Fe-Si liquidus surface in Fig. 9. The eutectic valleys L→α-Al + α-FeSi and L→α-Al + β-FeSi have been extrapolated to higher temperatures and lower Si content. In alloys cast by both methods, $Al_3Fe$ does not form and the solidification path lies on the extended α-Al liquidus moving from point A (initial composition) toward point B in the case of the D.C. ingot and toward point C in the case of the Hunter cast alloy. The volume fraction of dendritic α-Al in the two cases would be approximately 0.3 and 0.35 respectively. In practice due to other factors such as the shifting of the coupled zone [8] the volume fraction of dendritic phase could be much higher. This illustration clearly demonstrates the utility of metastable phase boundary extrapolation in the interpretation and analysis of RSP microstructure.

PRESSURE-TEMPERATURE DIAGRAMS

The attainment of information on the phase compositions and melting temperatures of possible metastable phases in binary systems by applying the extrapolation constructions to ternary alloys illustrates an important concept and practical result in the use of metastable phase diagrams. The application of this concept can be extended to include other intensive and extensive thermodynamic variables such as pressure. Indeed there is a fairly extensive experience demonstrating that at high pressure many metals and compounds exhibit structural modifications. With a pressure-temperature diagram for a given phase the metastable melting temperature and/or metastable allotropic transformation temperature at 1 atm. can be estimated for structural modifications normally existing only at high pressure [37].

As a general rule, the application of high pressure P may be expected to favor denser phases because of the effect of (PΔV) on the free energy. For most metallic phases the molar volume is roughly 10 $cm^3$ and volume changes, ΔV, associated with structural transitions are usually less than about 5% so that the change in molar free energy associated with a pressure of 50 Kbar is about 600 cal/mole. During RSP the change in free energy due to thermal undercooling is well represented by $\Delta H_m (\Delta T/T_m)$ where $\Delta H_m$ is the heat of fusion and ΔT is the thermal undercooling below the melting temperature [11]. With a thermal undercooling of $0.3 T_m$, which is within the range of RSP, and average $\Delta H_m$ of 2 Kcal/mole, the phases that can be stabilized by high pressure in the range up to about 50 Kbar should be considered as possible metastable phases during RSP.

There appears to be an increasing number of examples of metastable metallic phases produced by RSP which also become stable equilibrium phases at elevated pressure. One example is illustrated in Fig. 10 for Bi. At sufficiently large undercooling ($\Delta T = 0.41 T_m$), the metastable Bi(II) phase product forms from the melt in place of the stable Bi(I) phase [6]. The Bi (II) phase is observed
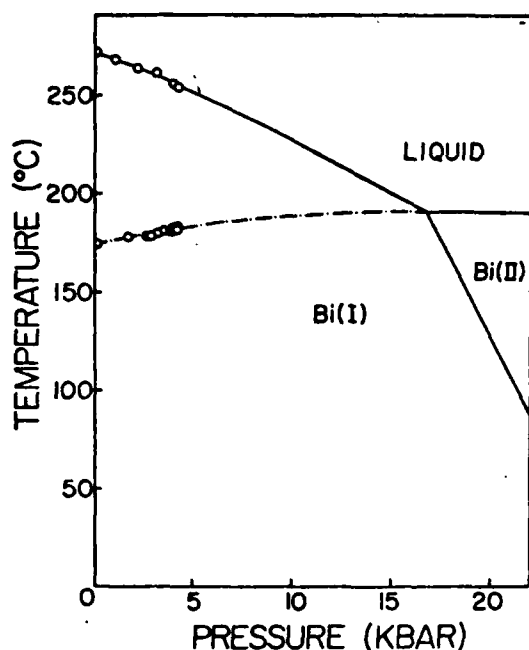
25

Fig. 10. Pressure-temperature diagram for Bi [38]. The dashed curve shows the estimated metastable melting point of Bi(II) as a function of pressure. The data shows the measured melting point of the Bi(II) phase formed at large undercooling by the droplet-emulsion technique [39].

to melt at 174 °C at 1 atm. An extrapolation of the pressure dependence of the Bi(II) melting temperature to 1 atm. yields a metastable melting temperature in close agreement with the observed value, especially when the measured pressure dependence of the metastable melting temperature [39] is considered. Similar observations have been reported for Ga [40] and Sb [41] as well as for a number of binary alloy systems such as Pb-Bi [42], Pb-Sb [43], In-Bi [44] and others. The incorporation of information on high pressure phases should prove to be quite useful not only in the interpretation of RSP product structures, but also in the anlysis of decomposition reactions during post-solidification treatment. Further, in the case of binary alloys the extrapolation of high pressure equilibrium to 1 atm. can provide information which is similar to that derived from ternary constructions. Since the addition of a ternary solute or the application of pressure can favor different phases, it is important to examine all sources of phase diagram information in order to develop the full range of metastable equilibria in a system.

THE $T_o$ CURVE

The discussion of phase diagram features of interest in RSP has been restricted so far to metastable equilibrium between phases. This metastability is important because of the difficulty of nucleating or growing a stable phase. However, in RSP there exists another form of non-equilibrium which is also important, and relates to non-equality of chemical potentials across an interface growing at a high rate and large undercooling. These rapid growth rates can trap the solute into the freezing solid at levels exceeding the equilibrium value for the corresponding liquid composition present at the interface. The increase in chemical potential of the solute across the interface must be balanced by the decrease in chemical potential of the solvent in order for crystallization to occur [11]. To achieve this, the interface temperature must lie significantly below the liquidus temperature, whether stable or metastable. In the limit of partitionless solidification, i.e., where the composition of the solid equals the composition of the liquid at the interface, a thermodynamic temperature exists which is the highest interface temperature at which partitionless solidification can occur. This temperature is called the $T_0$ temperature and is the
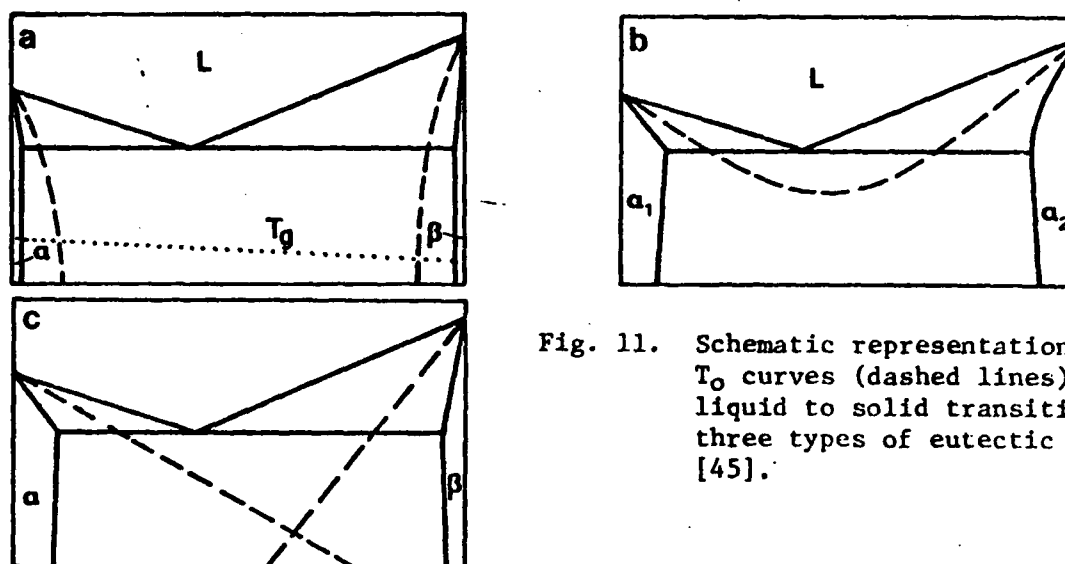
26

Fig. 11. Schematic representation of the $T_0$ curves (dashed lines) for the liquid to solid transition for three types of eutectic system [45].

temperature at which the molar free energies of the liquid and solid phase are equal for the given composition. The locus of $T_0$ over a range of composition constitutes a $T_0$ curve and represents an important piece of thermodynamic data which should be included whenever possible in phase diagrams calculations.

The geometrical structure of $T_0$ curves can be considered by illustration on a few simple phase diagrams with reference to RSP phenomena. The $T_0$ curves exist, of course, for the liquid with both stable or metastable phases, and lie between the liquidus and solidus. Figure 11 shows schematically, possible $T_0$ curves for three simple eutectic phase diagrams [45]. One important use of this curve is to determine whether a bound exists for the extension of solubility by rapid melt quenching. If the $T_0$ curve plunges to very low temperature at some composition as seen in Fig. 11a, the single phase with composition beyond the $T_0$ curve cannot be formed from the melt. In fact, for systems with retrograde solubility [46], the $T_0$ curve seems to plunge to absolute zero at a composition equal to the liquidus composition at the retrograde temperature. Experiments on laser melted Si seem to confirm this. Moreover, eutectic alloys with plunging $T_0$ curves are good candidates for easy metallic glass formation [47,48].

In contrast, alloys with the $T_0$ curve type of Fig. 11b, which is only slightly depressed below the stable liquidus curves, make a good candidate for solubility extension. The Ag–Cu system has such a $T_0$ curve and has long been known [49] to form a series of FCC solid solutions from the melt across the entire binary diagram by rapid quenching. Another possible structure for the $T_0$ curve is shown in Fig. 11c.

In Fig. 12 the $T_0$ and spinodal curves are represented as well as the metastable phase boundaries in a liquid miscibility gap system. The unstable branches of the phase boundaries are shown only for geometrical complete-ness. This diagram shows that the $T_0$ curve can pass smoothly through the spinodal for the liquid phase. It seems unlikely, however, that extension of solubility of the solid phase beyond this intersection would be possible. Spinodal decomposition, which requires no nucleation step would prevent the parent (liquid) phase from existing as a homogeneous solution beyond the inter-section. In contrast, it is interesting to note that the presence of a spinodal in the product (solid) phase does not limit the extension of solid solubility from the melt during RSP as demonstrated in the Ag–Cu system. Subsequently, spinodal decomposition may occur in the solid [50]. This figure also demonstrates the fact that metastable phase boundaries do not extend beyond spinodals. In this case the liquidus and solidus emerge from the other side of the spinodal as metastable phase boundaries [51,52].
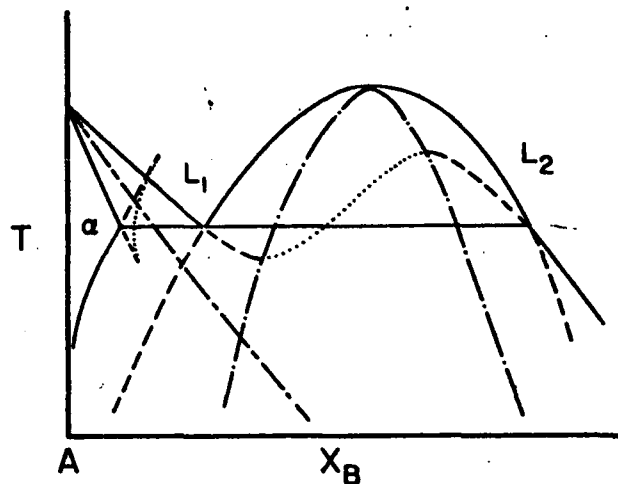
27

Fig. 12. Metastable phase boundaries (dashed), spinodal curve for the liquid miscibility gap (dashed-dot) and the $T_O$ curve for the L to $\alpha$ transformation (long-short dashed) for a monotectic diagram. The metastable phase boundaries become unstable (dotted) when they reach the spinodal. Extension of solid solubility beyond the composition of the intersection of the $T_O$ curve with the liquid phase spinodal seems unlikely.

## SUMMARY

1.  Phase diagrams can be used in developing an understanding of the thermo-dynamic conditions involved in metastable phase formation. Often RSP product structures which are not readily understood in the context of the stable equilibrium diagram can have a straightforward interpretation based on a metastable phase diagram.

2.  Useful first-level information on metastable phases such as melting temperature, location of metastable invariant reactions and possible metastable intermediate phases can be obtained by graphical extrapolations of equilibrium phase boundaries.

3.  A complete assessment of metastable phase equilibria requires a consideration of phase stability based upon analytical free energy functions.

4.  An effective RSP strategy and alloy design should incorporate the considera-tion of a metastable phase diagram together with a solidification kinetics analysis.

## REFERENCES

1.  M. C. Flemings, Solidification Processing (McGraw-Hill, New York, 1974).
2.  D. Turnbull, J. Chem. Phys., 20 411 (1952); Contemp. Phys., 10 473 (1969).
3.  J. W. Christian, The Theory of Transformations in Metals and Alloys, (Pergamon Press, Oxford, 1965).
4.  L. Bosio, A. Defrain and I. Epelboin, J. de Phys. 27, 61 (1966).
5.  J. H. Perepezko, in Rapid Solidification Processing: Principles and Technologies II, R. Mehrabian, B. H. Kear and M. Cohen, eds. (Claitor's Pub., Baton Rouge, LA, 1980) 56.

6. J. H. Perepezko and I. E. Anderson, in Synthesis and Properties of Metastable Phases, E. S. Machlin and T. J. Rowland, eds. (TMS-AIME, Warrendale, PA 1980), 31.
7. J. W. Cahn, W. B. Hillig and G. W. Sears, Acta Met. 12 1421 (1964).
8. W. Kurz and D. Fisher, Int. Met. Rev. 5-6 177 (1979).
9. C. M. Adam and L. M. Hogan, J. Australian Inst. of Metals 17 81 (1972).
10. I. R. Hughes and H. Jones, J. Mat. Sci. 11 1781 (1976).
11. J. C. Baker and J. W. Cahn, in Solidification (ASM, Metals Park, Ohio 1971), pp. 23-58.
12. M. Cohen, B. H. Kear and R. Mehrabian, in Rapid Solidification Processing: Principles and Technologies II, R. Behrabian, B. H. Kear and M. Cohen, eds. (Claitor's Pub., Baton Rouge, LA 1980), pp. 1-23.
13. B. Pieraggi and F. Dabosi, J. Mat. Sci. 14, 416 (1979).
14. M. Hillert, in Solidification and Casting of Metals (The Metals Society, London 1979), p. 81 and 157.
15. R. Hultgren, P. D. Desai, D. T. Hawkins, M. Glesier, K. K. Kelley and D. D. Wagman, Selected Values of Thermodynamic Properties of the Elements (ASM, Metals Park, Ohio 1973).
16. M. Hansen and K. Anderko, Constitution of Binary Alloys (McGraw-Hill, New York, 1958).
17. Metals Handbook, 8th Edition, 8 (ASM, Metals Park, Ohio 1973).
18. R. E. Cech, J. Metals 206, 585 (1956).
19. P. K. Srivastava, B. C. Giessen and N. J. Grant, Acta Met. 16 1199 (1968).
20. W. J. Boettinger, Met. Trans. 5, 2023 (1974).
21. H. D. Brody and S. A. David, in Solidification and Casting of Metals (The Metals Society, London 1979), p. 144.
22. L. Kaufman and H. Bernstein, Computer Calculations of Phase Diagrams (Academic Press, New York, 1970).
23. J. W. Cahn, Trans. TMS-AIME 242 168 (1968).
24. D. E. Polk and B. C. Giessen, in Metallic Glasses (ACM, Metals Park, Ohio 1978), pp. 1-35.
25. For example, D. A. Goodman, J. W. Cahn and L. H. Bennett, Bull. Alloy Phase Diag. 2, 29 (1981).
26. L. S. Darken and R. W. Gurry, Physical Chemistry of Metals, (McGraw-Hill, New York 1953).
27. W. J. Boettinger and J. H. Perepezko, unpublished work.
28. Y. Nakagawa, Acta Met. 6, 704 (1958).
29. J. D. Verhoeven and E. D. Gibson, J. Mat. Sci. 13, 1576 (1978).
30. F. Spaepen and D. Turnbull, in Metallic Glasses (ASM, Metals Park, Ohio 1978), pp. 114-127.
31. H.W.L. Phillips, Annotated Equilibrium Diagrams of Some Aluminum Alloy Systems (The Institute of Metals, London, 1959).
32. J. J. Richmond, J. H. Perepezko, S. E. LeBeau and K. P. Cooper, in Rapid Solidification Processing: Principles and Technologies III, NBS (in press).
33. C. J. Simensen and R. Vellesamy, Z. Metallkde. 68 428 (1977).
34. A. Tonejc, D. Rocak and A. Bouefacic, Acta Met. 19 311 (1971).
35. D. Duzevic, Scripta Met. 9, 543 (1975).
36. L. R. Morris, in Solidification and Casting of Metals (The Metals Society, London 1979), 218.
37. L. Kaufman, in Solids Under Pressure, M. Paul and D. M. Warschauer, eds. (McGraw-Hill, New York 1963), 304.
38. W. Klement, A. Jayaraman and G. C. Kennedy, Phys. Rev. 131 632 (1963).
39. D. LaCourt, J. S. Paik and J. H. Perepezko, to be published.
40. L. Bosio, A. Defrain and M. Dupont, J. Chim. Phys. 68 542 (1971).
41. D. Akhtar, V. D. Vankar, T. C. Goel and K. L. Chopra, J. Mat. Sci. 14 2422 (1979).
42. Ye. G. Ponyatovskiy and A. G. Rabinkin, Fiz. Metal. Metalloved. 30 606 (1970).

43. J. B. Clark and C.W.F.T. Pistorius, J. Less Common Metals, 42 59 (1975).

44. P. W. Richter, E. Rapoport and J. B. Clark, J. Less Common Metals, 60 195 (1978).

45. W. J. Boettinger, in Rapidly Solidified Amorphous and Crystalline Alloys, B. H. Kear, B. C. Giessen and M. Cohen, eds. (Elsevier, New York 1982), 15.

46. J. W. Cahn, S. R. Coriell and W. J. Boettinger, in Laser and Electron Beam Processing of Materials, C. W. White and P. S. Peercy, eds. (Academic Press, New York 1980), 89.

47. W. J. Boettinger, in Proc. of Fourth Int. Conf. on Rapidly Quenched Metals, T. Masumoto and K. Suzuki, eds. (Jap. Inst. Metals, Sendai 1982), 99.

48. T. B. Massalski, these proceedings.

49. P. Duwez, R. H. Willens and W. Klement, J. Appl. Phys. 31, 1136, 1500 (1960).

50. P. G. Boswell and G. A. Chadwick, J. Mat. Sci. 12, 1979 (1977).

51. M. Hillert, in Conference on In-Situ Composites-III (Ginn Custom Pub., Lexington, MA 1979), 48

52. J. W. Cahn, private communication.

OSCILLATORY MORPHOLOGICAL INSTABILITIES DUE TO NON-EQUILIBRIUM SEGREGATION

S.-R. Coriell
National Bureau of Standards
Washington, DC  20234

and

R. F. Sekerka*
Carnegie-Mellon University
Pittsburgh, PA  15213

Abstract

Linear perturbation theory is used to study morphological instability for rapid directional solidification at constant velocity under conditions where there is significant departure from local equilibrium at an initially planar solid-liquid interface.  Under conditions where the segregation coefficient $k$ depends significantly on velocity $v$, the stability criterion depends explicitly on both $k$ and $\partial k/\partial v$ and instabilities that are oscillatory in time can occur for solute concentrations that are much smaller than those that would be necessary to cause non-oscillatory instability for the same $k$ if $\partial k/\partial v$ were simply neglected.  Such oscillatory instabilities seem to be related to a "solute pump" mechanism according to which local changes in $k$, due to periodic changes in local interface velocity $v$, can occur out of phase with local interface position, thus resulting in lateral inhomogeneity of concentration on a length scale large enough that the resulting instabilities will not be suppressed by capillarity.  Such instabilities can, however, be suppressed by a sufficiently large dependence of interface undercooling on $v$.  When present, oscillatory instabilities lead to a three dimensional segregation pattern in which periodic solute variations in the two transverse directions are modulated by a periodic variation in the direction of growth.

---

* Consultant, National Bureau of Standards

## Introduction

Recent advances in the technology of rapid solidification, e.g., laser or electron beam melting and refreezing of thin layers on substrates, have focused increased attention on the phenomenon of morphological stability at rapid solidification rates [1,2]. This is especially true in view of the fact that classical theory [3] predicts absolute stability - i.e., stability for any solute concentration and any positive temperature gradient - provided that the velocity exceeds some critical value. It is expected, however, that there will be significant departures from local equilibrium for solidification at rapid rates and, hence, that classical stability theory will have to be modified; some steps in this direction have already been taken [4].

One of the more dramatic manifestations of the departure from equilibrium at rapid rates is the non-equilibrium partitioning of solute [5] as may be characterized by a non-equilibrium value of the distribution coefficient k, which is the ratio of solute concentration in the solid to that in the immediately adjacent liquid from which it freezes. The equilibrium value of k, namely $k_e$, is of thermodynamic origin but the non-equilibrium value of k can only be measured experimentally or calculated from a model based on kinetics. Several models [6-8] have been advanced recently but none have yet been subjected to careful scrutiny because of the limited amount of available experimental data. Nevertheless, measured values [1,2] of k for silicon have differed by orders of magnitude from $k_e$ for solidification rates of the order of a few meters/second and such differences would be expected to have a dramatic effect on morphological stability.

One way of attempting to account for the effect of a non-equilibrium value of k on morphological stability would be simply to substitute the value of k measured at the velocity of the unperturbed state in the classical analysis. In fact, the critical value of the velocity for absolute stability is proportional to $k/(1-k)$ so a big effect

might be expected. However, such a procedure of substitution of the actual value of k is not strictly correct. This follows because the actual non-equilibrium value of k arises from departures from local equilibrium at the solid-liquid interface and these must be accounted for systematically in the stability analysis. In particular, the local changes in velocity, v, that accompany the presence of a shape perturbation will give rise to local changes in k and these will affect stability.

We have, therefore, undertaken a linear stability analysis for solidification at a constant, but possibly very rapid, velocity of an initially planar solid-liquid interface while allowing for departures from local equilibrium that would be consistent with a non-equilibrium value of k. The analysis is accomplished by expanding about the unperturbed situation via linear perturbation theory and this procedure calls for information about k and its derivatives, for instance $k_v \equiv \partial k/\partial v$.

In the classical analysis of morphological stability, an unstable sinusoidally shaped perturbation grows exponentially in time while a stable perturbation decays in time. This decay can either be monotonic or oscillatory [9,10] but little attention has been paid to decaying oscillatory modes. In the present analysis, however, it will be found that the departure from local equilibrium, and especially a non-zero value of $k_v$, can lead to unstable oscillatory modes at solute concentrations possibly far below those at which a non-oscillatory mode would be expected to become unstable. Were it not for the possibility of these unstable oscillatory modes, the simple procedure of substitution of the actual value of k in the classical expressions would be correct.

## Theory

We consider the morphological stability of a planar solid-liquid interface during unidirectional solidification of a binary alloy at constant velocity V. We outline a standard linear time dependent stability analysis and then focus our attention to large velocities where non-equilibrium effects are likely.

We choose an $(x,y,z)$ coordinate system (moving with the planar interface) such that the solid-liquid interface is described by $z = W(x,y,t)$ where t is the time. We assume that $W(x,y,t)$ and any of its derivatives are sufficiently small that any nonlinear terms can be neglected.

We solve the differential equations

$$(\partial T_L/\partial t) = \kappa_L \nabla^2 T_L + V(\partial T_L/\partial z), \qquad (1a)$$

$$(\partial T_S/\partial t) = \kappa_S \nabla^2 T_S + V(\partial T_S/\partial z), \qquad (1b)$$

$$(\partial c/\partial t) = D\nabla^2 c + V(\partial c/\partial z), \qquad (1c)$$

where $T_L$ and $T_S$ are temperatures in the liquid and solid, respectively, c is the concentration of solute in the liquid (diffusion in the solid is neglected), $\kappa_L$ and $\kappa_S$ are thermal diffusivities of liquid and solid, respectively, and D is the diffusion coefficient of solute in the liquid.

The boundary conditions far from the solid-liquid interface are

$$(\partial T_L/\partial z) = G_L \exp(-Vz/\kappa_L) \qquad z \to \infty, \qquad (2a)$$

$$(\partial T_S/\partial z) = G_S \exp(-Vz/\kappa_S) \qquad z \to -\infty, \qquad (2b)$$

$$c = c_\infty \qquad z \to \infty, \qquad (2c)$$

where the temperature gradients $G_L$ and $G_s$ and the solute concentration $c_\infty$ are constants. We consider $G_s \geq 0$ and $G_L \geq 0$.

The boundary conditions at the solid-liquid interface are

$$T_L = T_s \tag{3a}$$

$$v = (k_s/L_v)(\partial T_s/\partial z) - (k_L/L_v)(\partial T_L/\partial z) \tag{3b}$$

$$v = - D(\partial c/\partial z)/(c-c_s) \tag{3c}$$

$$v = f(T_e-T_I, c_I, T_I) \tag{3d}$$

$$c_{sI} = c_I k(v, c_I, T_I) \tag{3e}$$

$$T_e \equiv T_M - T_M \Gamma K + g(c) \tag{3f}$$

where $v = V + (\partial W/\partial t)$ is the interface velocity, $k_s$ and $k_L$ are thermal conductivities of solid and liquid, respectively, $L_v$ is the latent heat per unit volume, $c_s$ is the concentration in the solid at the interface, $T_M$ is the melting point of a flat interface in the absence of solute, $\Gamma$ is the ratio of the solid-liquid surface tension $\gamma$ to the latent heat per unit volume, $K = - (\partial^2 W/\partial x^2) - (\partial^2 W/\partial y^2)$ is the interface curvature, the dependence of melting point on solute is given by the function $g(c)$, and the subscript I indicates evaluation at the solid-liquid interface. The departure from local equilibrium is determined by the functions $f(T_e-T_I, c_I, T_I)$ and $k(v, c_I, T_I)$; we require that if $v = 0$, then $T_e = T_I$ and $k = k_e$. We define the following partial derivatives of the functions f and k evaluated at values of the variables corresponding to the planar solid-liquid interface: $\mu_T = \partial f/\partial (T_e-T_I)$, $\mu_c = \partial f/\partial c_I$, $\mu_A = \partial f/\partial T_I$, $k_c = \partial k/\partial$ $k_v = \partial k/\partial v$, and $k_A = \partial k/\partial T_I$. We note that $k_c$ defined here is not the

same quantity as in our previous paper [4] where we wrote $c_{sI} = h(c_I, T_e-T_I)$ and $k_c$ represented $\partial c_{sI}/\partial c_I$. In equation (3b) we have omitted corrections that might arise from consideration of surface entropy and also a possible dependence of $g(c)$ on curvature.

In carrying out a linear stability analysis, we write each of the temperature and concentration fields as a sum of an unperturbed part, which is a function of z alone, and a perturbed part which is of the form $F_j(z) \exp[\sigma t + i(\omega_x x + \omega_y y)]$. The perturbed solid-liquid interface is given by

$$z = W(x,y,t) = \delta \exp[\sigma t + i(\omega_x x + \omega_y y)], \tag{4}$$

where $\delta$ is the perturbation amplitude at $t = 0$, and $\omega_x$ and $\omega_y$ are spatial frequencies. The above expressions for the perturbed interface and fields are written with the understanding that actual quantities are the real parts of the corresponding complex expressions, a procedure that is permissible because of our use of linear perturbation theory. The interface is unstable if the real part of the rate parameter $\sigma$ is positive for any perturbation, i.e., any real values of $\omega_x$ and $\omega_y$. The interface is stable if the real part of $\sigma$ is negative for all perturbations.

Upon solving the differential equations, we find

$$\sigma = V\{[-k_L G_L(\alpha_L - V/\kappa_L) - k_s G_s(\alpha_s + V/\kappa_s)]U_A - 2\overline{k}T_M \Gamma \omega^2 \overline{\alpha}$$

$$+ 2\overline{k}m'G_c\overline{\alpha}(\alpha - V/D)/(\alpha - p'V/D)\}/\{L_v V U_T$$

$$+ [2\overline{k}m'G_c\overline{\alpha}/(\alpha - p'V/D)]U_K\}, \tag{5}$$

with

$$\alpha = (V/2D) + [(V/2D)^2 + \omega^2 + \sigma/D]^{\frac{1}{2}},$$

$$\alpha_L = (V/2\kappa_L) + [(V/2\kappa_L)^2 + \omega^2 + \sigma/\kappa_L]^{\frac{1}{2}}$$

36

$$\alpha_s = -(V/2\kappa_s) + [(V/2\kappa_s)^2 + \omega^2 + \sigma/\kappa_s]^{\frac{1}{2}}$$

$$\bar{\alpha} = (k_s\alpha_s + k_L\alpha_L)/(2\bar{k}),$$

$$2\bar{k} = k_s + k_L,$$

$$\omega^2 = \omega_x^2 + \omega_y^2,$$

$$G_c = Vc_0(k-1)/D,$$

$$m' = (dg/dc) + \mu_c/\mu_T,$$

$$p' = 1 - k - c_0k_c,$$

$$U_A = 1 - (\mu_A/\mu_T) + (Vc_0m'k_A/D)/(\alpha - Vp'/D),$$

$$U_T = 1 - (\mu_A/\mu_T) + 2\bar{k}\,\bar{\alpha}/(L_V\mu_T),$$

and

$$U_K = 1 - [Vk_V/(1-k)] - VL_Vk_A/[(1-k)2\bar{k}\,\bar{\alpha}],$$

where $c_0$ and $k$ in these expressions are, respectively, the interface concentration
in the liquid and the distribution coefficient for the unperturbed interface
growing at velocity V. Note that k will generally be different from the
equilibrium distribution coefficient $k_e$. We note that in the definitions of $\alpha$, $\alpha_L$, and
$\alpha_s$, we require that the real part of the square root be positive in order to
satisfy the boundary conditions at infinity.

The perturbation wavelength, $\lambda = 2\pi/\omega$, at the onset of instability is
sufficiently small that $\omega \gg (V/2\kappa_s)$ and $\omega \gg (V/2\kappa_L)$. Hence we may use the
thermal steady state approximation and let the thermal diffusivities approach
infinity. We further simplify the problem by taking $\mu_A = k_A = 0$. We then
write equation (5) as

$$\Sigma = n\{-(Q+Pn^2) + I(R-\tfrac{1}{2})/(R+\tfrac{1}{2}-p')\}/$$

$$\{1 + Mn + I(1-H)n/(R+\tfrac{1}{2}-p')\},$$

(6)

where we have introduced the dimensionless variables

$$\Sigma = \sigma D/V^2, \qquad \text{(rate parameter)}$$

$$\eta = D\omega/V, \qquad \text{(wavenumber)}$$

$$R = (\tfrac{1}{4}+\eta^2+\Sigma)^{\frac{1}{2}},$$

$$Q = (k_L G_L + k_S G_S)/(L_V V), \qquad \text{(dimensionless ratio of temperature gradient to growth rate)}$$

$$P = 2\bar{k}T_M \Gamma V/(L_V D^2), \qquad \text{(capillarity parameter)}$$

$$I = 2\bar{k}m'G_c/(L_V V), \qquad \text{(concentration parameter)}$$

$$M = 2\bar{k}V/(L_V \mu_T D), \qquad \text{(interface undercooling parameter)}$$

and

$$H = Vk_V/(1-k). \qquad \text{(non-equilibrium segregation rate parameter)}$$

We require that the real part of R be positive in order to satisfy the boundary conditions on the perturbed concentration field at infinity.

The interface is stable if the real part of $\Sigma$ is negative for all values of $\eta$. From equation (6) it is clear that $\Sigma(\eta)$ depends on the six dimensionless variables Q, P, I, p', M, and H. When local equilibrium holds at the solid-liquid interface, both M and H vanish. Thus, one effect of deviations from local equilibrium is to modify the denominator on the right hand side of equation (6). Further, if $\Sigma$ is real, then the zeroes of equation (6) are determined by the zeroes of the numerator on the right hand side of equation (6). Since the numerator is independent of M and H and has the same functional form as in the local equilibrium case, the classical analysis applies. Of course, $I = 2\bar{k}m'c_\infty(k-1)/(L_V Dk)$ may be considerably different from the local equilibrium value if k deviates appreciably from the equilibrium distribution

38

coefficient, $k_e$. Thus, if $\Sigma$ is real at the stability-instability demarcation, the usual morphological stability results hold but with the equilibrium distribution coefficient replaced by the actual distribution coefficient (more precisely the equilibrium values of I and $p'$ replaced by their actual values). While the numerator depends on the four dimensionless variables Q, P, I, and $p'$, the zeroes of the numerator depend only on the three variables I/P, Q/P and $p'$. We also define the dimensionless variable $A = kP/I$, which is identical to the absolute stability variable A in the case of local equilibrium [3].

We now proceed to investigate the possibility of oscillatory instabilities, i.e., the imaginary part of $\Sigma$ is non-vanishing. Since $\Sigma = R^2 - (\frac{1}{4} + n^2)$, equation (6) can be written as a cubic polynomial in R, viz.

$$a_3 R^3 + a_2 R^2 + a_1 R + a_0 = 0, \tag{7}$$

where

$$a_3 = 1 + Mn$$

$$a_2 = a_3(\frac{1}{2} - p') + I(1-H)n$$

$$a_1 = n(Q + Pn^2 - I) - (\frac{1}{4} + n^2)a_3$$

$$a_0 = n(Q + Pn^2)(\frac{1}{2} - p') + \frac{1}{2}nI - (\frac{1}{4} + n^2)a_2.$$

Clearly, there are three roots of equation (7); however, some or all of these may be excluded by the condition that the real part of R be positive. Thus, for a given value of n, there are three or less values of $\Sigma$. There are either three real roots of equation (7) or one real root and two complex conjugate roots. Hence if $\Sigma$ is complex root of equation (6), the complex conjugate $\Sigma^*$ is also a root.

We will only consider the situation in which $1 - p' = k + c_0 k_c > 0$, $M > 0$, and $I \geq 0$. Violation of these inequalities during crystal growth appears unlikely. In order to demonstrate some general properties of equation (6), we rewrite it in the form

$$\Sigma(a_3 R + a_2) = n\{(R - \tfrac{1}{2})J + (1-p')(J-I)\} \tag{8a}$$

where

$$J = I - (Q + P n^2).$$

We let $\Sigma \equiv \Sigma_R + i\Sigma_I = R^2 - (\tfrac{1}{4} + n^2) \equiv R_R^2 - R_I^2 - (\tfrac{1}{4} + n^2) + i2R_R R_I$, decompose equation (8a) into its real and imaginary parts and rearrange terms to obtain

$$\Sigma_R(a_3 R_R + a_2) - a_3 \Sigma_I R_I = n\{(R_R - \tfrac{1}{2})J + (1 - p')(J - I)\} \tag{8b}$$

and

$$R_I\{2R_R(a_3 R_R + a_2)\} = R_I\{-a_3 \Sigma_R + nJ\}. \tag{8c}$$

We shall proceed to prove that if $H < 1$ and $I \leq Q$, which just happens to be the modified constitutional supercooling criterion for stability [3], that the system is stable against both non-oscillatory ($\Sigma_I = 0$) and oscillatory ($\Sigma_I \neq 0$) modes.

The proof is as follows:

If $(a_3 R_R + a_2) > 0$ and $J \leq 0$, then we shall show that there are no solutions to equation (8) for $\Sigma_R > 0$, and hence there is stability. The variable $n$ is non-negative; for $\Sigma_R > 0$, $R_R = (\Sigma_R + R_I^2 + \tfrac{1}{4} + n^2)^{\frac{1}{2}} > \tfrac{1}{2}$ and hence $R_R - \tfrac{1}{2} > 0$. If $R_I = 0$, the right hand side of equation (8b) is negative while the left hand side is positive, and hence there is no solution. If $R_I \neq 0$, the factor multiplying $R_I$ on the right hand side of equation (8c) is negative while the corresponding factor on the left hand side is positive, and again there is no solution. For

40

$\Sigma_R > 0$, the quantity $a_3 R_R + a_2 > a_3 \frac{1}{2} + a_2 = a_3(1 - p') + I(1 - H)n$. Hence $a_3 R_R + a_2 > 0$ if $H < 1$. Since $J \leq 0$ if $I \leq Q$, we have the result that for $H < 1$ and $I \leq Q$, the system is stable.

## Results

We will present a number of results in graphical form. Before proceeding we estimate the range of values of the dimensionless varibles. We are primarily interested in rapid solidification where significant deviations from local equilibrium are most likely. During the regrowth process, which follows surface melting by a laser or electron beam, the temperature gradient in the liquid is considerably smaller than the gradient in the solid. If we neglect the gradient in the liquid, then $Q = [1+(k_L G_L)/(k_S G_S)]/[1-(k_L G_L)/(k_S G_S)] \cong 1.0$. We will use this value of $Q$ in our calculations.

For silicon, using the data of reference 1, we have $P = 4.5 (10^{-3})V$ with $V$ in cm/s. For aluminum, using the data of reference 4, we have $P = 11V$. This three order of magnitude difference between the $P$ values for silicon and aluminum for the same $V$ is due to the order of magnitude difference in diffusion coefficients and thermal conductivities. We have carried out calculations for $P$ in the range of 1 to $10^3$.

The dimensionless quantity $M/P = D/(T_M \Gamma \mu_T)$; since $T_M \Gamma \cong 10^{-5}$ Kcm for most materials, $M/P \cong 10^5 D/\mu_T$. Thus for silicon $M/P \cong 50/\mu_T$ while for aluminum $M/P \cong 5/\mu_T$ with $\mu_T$ in cm/(sK). The magnitude of $\mu_T$ is not well known; an upper bound on $\mu_T$ can be estimated from the speed of sound (11) and gives $\mu_T$ of the order of $10^2$ cm/(sK). For linear interface kinetics, this would correspond to 1.0K interface undercooling for $V = 10^2$ cm/s. However, for silicon, $\mu_T$ may be considerably smaller. Therefore, $M/P$ is probably greater than $5 \times 10^{-1}$ for silicon and $5 \times 10^{-2}$ for aluminum.

The variable $I$ depends on the solute concentration; in many of our computations we will regard $I$ as the dependent variable and calculate $I$ at the onset of instability as a function of $Q$, $P$, $p'$, $M$ and $H$.

41

For silicon, there is some experimental data on the distribution coefficient k as a function of velocity (1-2) and there are a number of models (6-8) relating the distribution coefficient to crystallization velocity. For our calculations we will simply fix $k = 1-p^* = 0.5$ (we neglect the dependence of k on $c_I$, i.e., we take $k_c = 0$) and vary $H = V(\partial k/\partial v)/(1-k)$ from 0 to 1. At present it is not clear how large H can become but in the models of references 6 and 8, H is bounded by unity.

Previous research [9-10] established that under conditions of local equilibrium at the solid-liquid interface, i.e., $H = M = 0$, there were stable $(\Sigma_R < 0)$ oscillatory roots of equation (6). This is illustrated in Figure 1, which gives $\Sigma_R$ and $\Sigma_I$ as functions of $\eta$. For $0.016 < \eta < 0.16$, $\Sigma_I$ is non-vanishing. For $\eta > 0.5$, there is only one allowed root which is real. For different values of the parameters, we have found ranges of $\eta$ for which there are no allowed roots. For the parameters of Figure 1, the variable $A = kP/I = 1$ which corresponds to the absolute stability criterion, which is sufficient for stability when local equilibrium holds.

In Figure 2, we use the same parameters as in Figure 1 except that we let $H = 0$, 0.04, and 0.1. The curve for $H = 0$ is identical to that of Figure 1 although the $\Sigma_R$ scale has been changed. As H increases from zero, the oscillatory roots become unstable, i.e., $\Sigma_R > 0$ and $\Sigma_I$ is non-vanishing. Since $A = 1$, we know from previous analysis [3] that $\Sigma = 0$ is not a root of equation (6). Thus $\Sigma_I \neq 0$ when $\Sigma_R = 0$ as indicated in Figure 2. Once $\Sigma_R > 0$, $\Sigma_I$ may vanish as occurs over a narrow range of $\eta$ for $H = 0.1$ in Figure 2.

In Figure 3, we illustrate the effect of deviations of interface temperature from the equilibrium temperature on the onset of instability. We have plotted $Q/(kP)$ as a function of $A^{-1} = I/(kP)$ for $Q = 1$, $k = \frac{1}{2}$ and $H = 1.0$ for various values of $M/P = D/(\mu_T T_M \Gamma)$, which depends only on the alloy properties and not on

the processing variables. When local equilibrium holds, $Q/(kP)$ as a function of $A^{-1}$ depends only on $k$, is independent of $Q$ and is identical to the curve labelled $M > 1.3P$. The absolute stability criterion is $A = 1.0$, i.e., a vertical line. Also shown in Figure 3 is the modified constitutional supercooling criterion, $I = Q$, or in dimensional variables, $(k_L G_L + k_s G_s)/(k_s + k_L) = m^- G_c$. In between the curve for local equilibrium and the line for the modified supercooling criterion are dashed curves corresponding to oscillatory instabilities, as would be expected from our proof based on equations (8). As the value of $M/P$ decreases, the difference between the $A^{-1}$ values for the onset of instability for non-oscillatory and oscillatory modes increases, with the largest differences occurring for large values of $P$ (small values of $Q/(kP)$).

From Figure 3, it is evident that large values of $M$ suppress oscillatory instability. The interaction between $H$ and $M$ is shown in Figures 4 and 5 for $P = 10^2$ and $10^3$, respectively. For fixed $M$, increasing $H$ promotes oscillatory instability which occurs at decreasing values of $A^{-1} = I/(kP)$ as $H$ increases. When $H = 0$, there is no oscillatory instability and the value of $A^{-1}$ is given by the horizontal line in Figures 4 and 5. As long as $H$ is sufficiently small or $M$ sufficiently large, there is no oscillatory instability and hence the value of $A^{-1}$ does not change and is still given by the horizontal line. For fixed $M$, when $H$ is above a certain critical value, oscillatory instability develops and with increasing $H$, $A^{-1}$ decreases.

When oscillatory instability occurs, the roots of equation (6) occur as complex conjugate pairs, i.e., if $\Sigma_R + i\Sigma_I$ is a root, then $\Sigma_R - i\Sigma_I$ is also a root. Hence, the $x$, $y$, and $t$ dependence of any of the perturbed quantities, e.g., interface shape or concentration, can be written in the form $\exp(\sigma_R t)$ $\cos(\omega_x x + \omega_y y) \cos(\sigma_I t)$ where $\sigma = \sigma_R + i\sigma_I$. The time for each oscillation is $2\pi/\sigma_I$ and during this time the unperturbed interface will have advanced a distance $2\pi V/\sigma_I$, which we define as the longitudinal wavelength in contrast to the transverse wavelength $2\pi/\omega$. Taking $D/V$ as the unit of length, we define a

dimensionless longitudinal wavelength $\lambda_\ell = 2\pi/\Sigma_I$ and a dimensionless transverse wavelength $\lambda_t = 2\pi/n$. For $Q = 1$, $k = \frac{1}{2}$, and $M = 0$, we show $\lambda_\ell$ and $\lambda_t$ as functions of $Q/(kP)$ for $H = 0.0$ and 1.0 in Figure 6. Of course, for $H = 0.0$ there is no oscillatory instability and $\lambda_\ell$ is infinite. For $H = 1.0$ the transverse wavelength is about 5 times larger than the longitudinal wavelength for small values of $Q/(kP)$. As $Q/(kP)$ increases, the transverse wavelength decreases while the longitudinal is approximately constant so that the two curves eventually cross. The transverse wavelength for $H = 1.0$ is larger than the transverse wavelength for $H = 0.0$, but both wavelengths are of the same order of magnitude.

## Conclusions

Departures from local equilibrium that occur at rapid rates of solidification and result in non-equilibrium distribution coefficients that depend on velocity can give rise to oscillatory morphological instabilities at solute concentrations that can be much smaller than those that would lead to non-oscillatory instabilities. These unstable oscillatory modes result from a non-zero value of $k_v = \partial k/\partial v$ but tend to be suppressed by sufficiently small values of the kinetic coefficient $\mu_T = \partial v/\partial(T_e - T_I)$. Although it is possible to calculate (see Figures 4-5) the value of $\mu_T$ needed to suppress the oscillatory instabilities related to $k_v$, our current knowledge of the actual relationship of $\mu_T$ to $k_v$ is too meager to determine whether such instabilities can occur in fact. For silicon freezing at 2 m/s, we estimate $P \sim 1$ so oscillatory instabilities can be suppressed by a value of $M = 0.1$ for $H = 1$. Nevertheless, we have every reason to suspect that oscillatory instabilities can exist for some alloys and experimental conditions.

The explanation of such oscillatory instabilities on the basis of a simple physical model is uncertain but we can make some conjectures. We suspect that such instabilities arise because of a "solute pump" effect according to which local

44

changes in interface velocity give rise to local changes in solute rejection or incorporation and this amounts t ocal solute redistribution without the need for lateral solute diffusion. Since lateral solute diffusion can occur only over short distances at high solidification rates, the potential concommitant instabilities become suppressed by capillarity, which is the reason for the "classical absolute stability criterion. But the existence of a local "solute pump" can allow a wavelength for oscillatory instability that is larger than the wavelengths that would be allowed by lateral solute diffusion alone. This larger wavelength is less stabilized by capillarity and the absolute stability criterion can be violated. We have shown, however, that for H < 1, instability never takes place (oscillatory or not) unless the modified constitutional supercooling principle is violated.

The fact that the instability that stems from the "solute pump" mechanism is oscillatory can be reconciled on the basis of a 90° phase difference between the local interface position and the local interface velocity at the onset of instability. This gives rise to a corresponding 90° phase difference between the local value of k and the local interface position. Thus, at the instant when an oscillating sinusoidal interface is planar, the distribution coefficient varies sinusoidally along it and the "locally pumped" solute varies likewise.

Even if the onset of instability is via an oscillatory mode, as it is in Figure 2, it is possible for non-oscillatory instabilities to exist as is evident near the maximum of the curve for H = 0.1. This is probably related to the fact that phase of the perturbed velocity differs from that of the perturbed interface shape by an angle arctan $(\sigma_I/\sigma_R)$ which is 90° for the onset of oscillatory instability but decreases as $\sigma_R$ increases. Therefore, the "solute pump" mechanism tends to become more in phase with the interface shape and, eventually, a non-oscillatory instability evidently prevails.

45

The solute concentration at a solid-liquid interface that is undergoing oscillatory instability may be expressed in the form

$$c = c_0 + \Delta c \exp(\sigma_R t) \cos(\omega_x x) \cos(\omega_y y) \cos(\sigma_I t + \phi) \tag{9}$$

where $\Delta c$ and $\phi$ represent an amplitude (proportional to $\delta$) and a phase that may be calculated but are not particularly interesting. To get the solute segregation pattern that would be consistent with equation (9), we simply replace t by $(z-z_0)/V$ where $z_0/V \equiv \phi/\sigma_I$ is chosen conveniently to simplify the final result. The resulting segregation pattern will then be proportional to

$$\exp(\sigma_R z/V) \cos(\omega_x x) \cos(\omega_y y) \cos(\sigma_i z/V) \tag{10a}$$

which, when expressed in dimensionless form, becomes

$$\exp(\Sigma_R Z) \cos(\eta_x X) \cos(\eta_y Y) \cos(\Sigma_I Z) \tag{10b}$$

where $(X, Y, Z) = (V/D)(x, y, z)$, $\eta_x = D\omega_x/V$ and $\eta_y = D\omega_y/V$. We note that $\lambda_\ell = 2\pi/\Sigma_I$ is the dimensionless longitudinal wavelength and $\lambda_t = 2\pi/(\eta_x^2 + \eta_y^2)^{1/2}$ is the dimensionless transverse wavelength, as defined previously and plotted in Figure 6. This segregation pattern should be compared to that for a non-oscillatory mode for which the factor of $\cos(\Sigma_I Z)$ would be missing. Thus the crucial distinguishing feature of a segregation pattern due to oscillatory instability rather than a non-oscillatory instability is the additional periodic modulation of the pattern in the growth direction.

Finally, we must emphasize that the calculations of this paper do not address the important general question of the effect of a higher but still constant value of V on instability. This can only be done if one adopts a specific model that allows k, $k_v$ and $\mu_T$ to change systematically together. In the calculations of this paper, we have simply taken $k = \frac{1}{2}$ and explored the effect of various values of $k_v$ and $\mu_T$.

## Acknowledgments

## References

1. A. G. Cullis, D.T.J. Hurle, H. C. Webber, N. G. Chew, J. M. Poate, P. Baeri, and G. Foti, Appl. Phys. Lett. $\underline{38}$, 642 (1981).

2. J. Narayan, H. Naramoto, and C. W. White, J. Appl. Phys. $\underline{53}$, 912 (1982).

3. W. W. Mullins and R. F. Sekerka, J. Appl. Phys. $\underline{35}$, 444 (1964).

4. S. R. Coriell and R. F. Sekerka, in: Rapid Solidification Processing Principles and Technologies, II, Eds. R. Mehrabian, B. H. Kear, and M. Cohen (Claitor, Baton Rouge, LA, 1980) p. 35.

5. J. C. Baker and J. W. Cahn, in: Solidification (Am. Soc. Metals, Metals Park, Ohio, 1970) p. 23.

6. K. A. Jackson, G. H. Gilmer, and H. J. Leamy, in: Laser and Electron Beam Processing of Materials, Eds. C. W. White and P. S. Peercy (Academic, New York, 1980) p. 104.

7. R. F. Wood, Phys. Rev. B $\underline{25}$, 2786 (1982).

8. M. J. Aziz, J. Appl. Phys. $\underline{53}$, 1158 (1982).

9. R. F. Sekerka, in: Crystal Growth, Ed. H. S. Peiser (Pergamon, Oxford, 1978) p. 691.

10. D. J. Wollkind, in: Preparation and Properties of Solid State Materials, Vol. 4, Ed. W. R. Wilcox (Marcel Dekker, New York, 1979) p. 111.

11. F. Spaepen and D. Turnbull, in: Rapidly Quenched Metals, Eds. N. J. Grant and B. C. Giessen (M.I.T. Press, Cambridge, MA, 1976) p. 205.

**Fig. 1.** The real and imaginary parts of $\Sigma = \sigma D/V^2$ as a function of $\eta = D\omega/V$ for a perturbation
of the solid-liquid interface of the form $\exp(\Sigma\Theta + i\eta X)$, for $Q = 1$,
$P = 10^3$, $k = \frac{1}{2}$, $M = H = 0$, and $I = 500$. Time $\Theta$ is measured in
units of $D/V^2$ and distance $X$ is measured in units of $D/V$. The real
part of $\Sigma$ is never positive so the system is stable. Dashed curves
correspond to complex values of $\Sigma$.

**Fig. 2.** The real part of $\Sigma$ as a function of the spatial frequency $\eta$ of a
sinusoidal perturbation for $H = V(\partial k/\partial v)/(1-k) = 0$, 0.04, and 0.1;
the other parameters are the same as in fig. 1. The solid and
dashed curves indicate vanishing and non-vanishing values of the
imaginary part of $\Sigma$, respectively. The interface is unstable for $H$
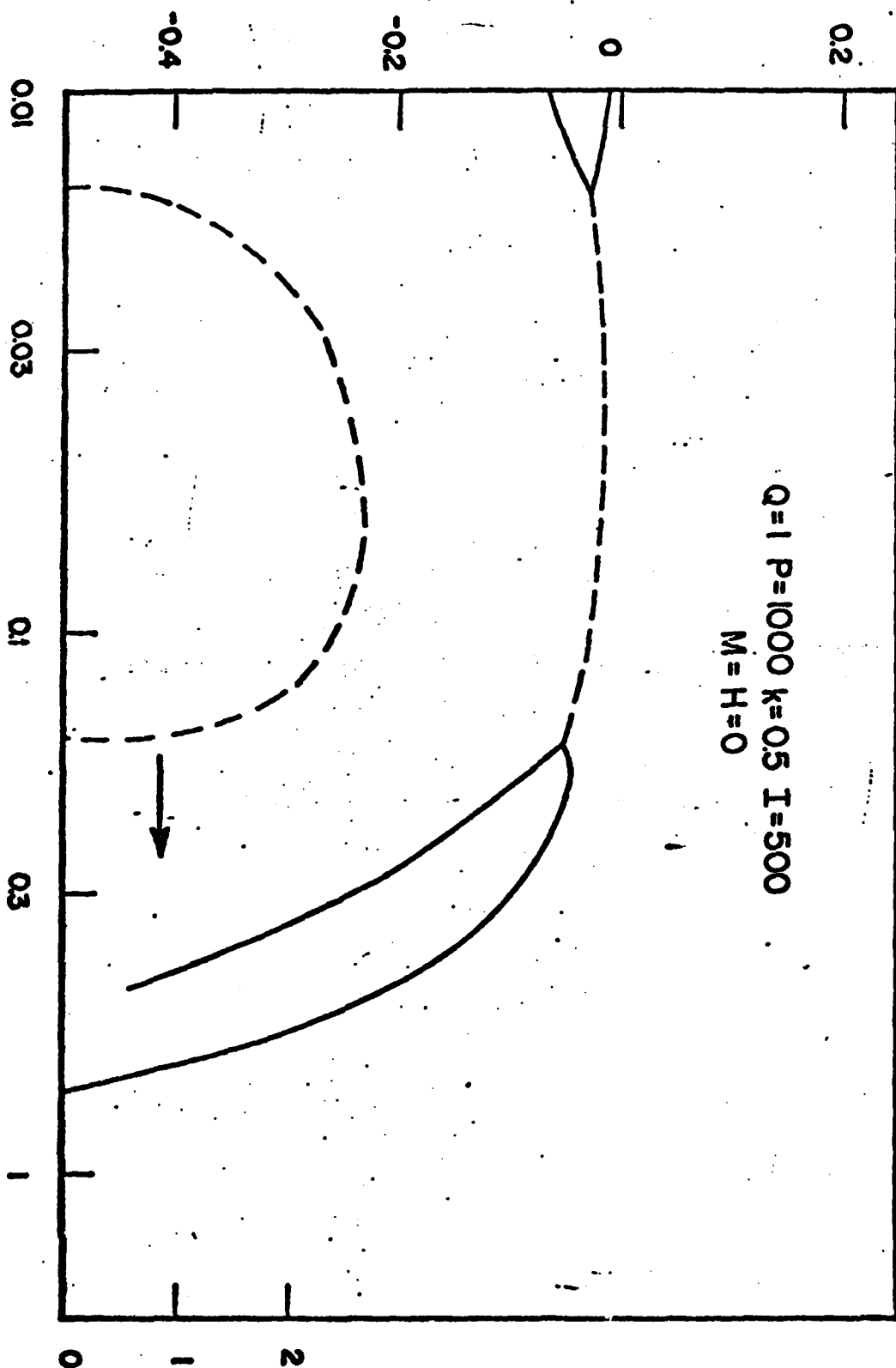= 0.1 and $H$ = 0.04 in which case the dashed curve peaks at $\Sigma = 3 \times 10^{-3}$.

**Fig. 3.** The dimensionless parameter $Q/(kP) = [(k_L G_L + k_s G_s)D^2]/[2\bar{k}T_M kV^2]$
as a function of $A^{-1} = I/(kP) = m'c_\infty(k-1)D/(k^2 T_M \Gamma V)$ on a logarithmic
scale for $Q = 1$, $k = \frac{1}{2}$, and $H = 1$ for different values of $M/P =$
$D/(T_M \Gamma \mu_T)$. The interface is unstable for values to the right of a
given curve. The line $I = Q$ corresponds to the modified constitutional
supercooling criterion, while $A = 1$ would correspond to absolute
stability. For $M > 1.3P$, the instability is non-oscillatory and
this curve is identical to that for $H = M = 0$. For other values of
$M$, the instabilities are oscillatory, and represented by dashed
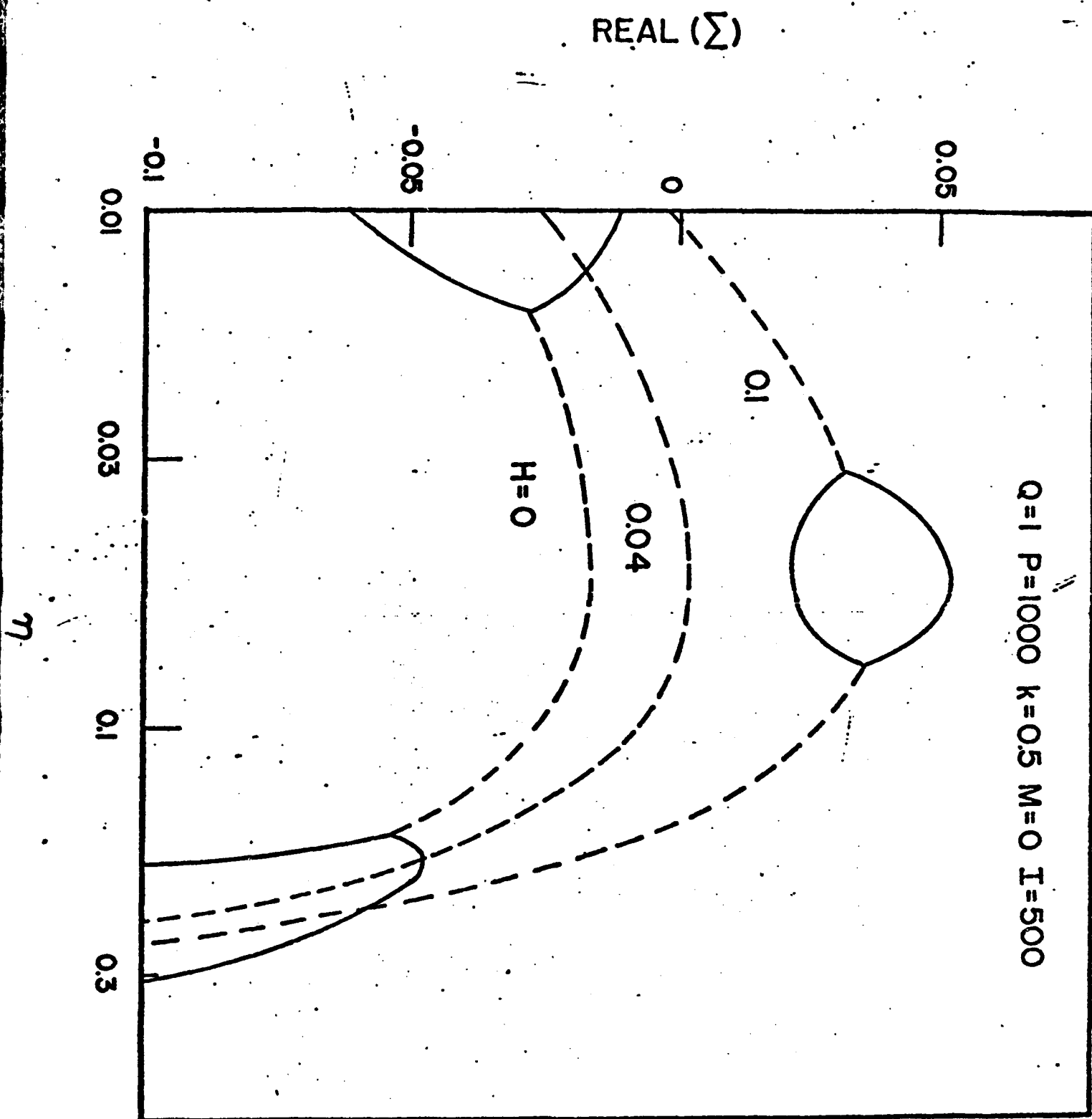curves.

Fig. 4. The dimensionless quantity $A^{-1} = I/(kP)$ as a function of $H = V(\partial k/\partial v)/(1-k)$ with $Q = 1$, $P = 10^2$, and $k = \frac{1}{2}$ for various values of M. The interface is unstable for values to the right of a given curve. The horizontal line gives the value of $A^{-1}$ for a non-oscillatory instability and oscillatory instabilities set in at the critical values of H where this line meets the dashed curves.

Fig. 5. The dimensionless quantity $A^{-1} = I/(kP)$ as a function of $H = V(\partial k/\partial v)/(1-k)$ with $Q = 1$, $P = 10^3$, and $k = \frac{1}{2}$ for various values of M. The interface is unstable for values to the right of a given curve. The horizontal line gives the values of $A^{-1}$ for a non-oscillatory instability and oscillatory instabilities set in at the critical values of H where this line meets the dashed curves.
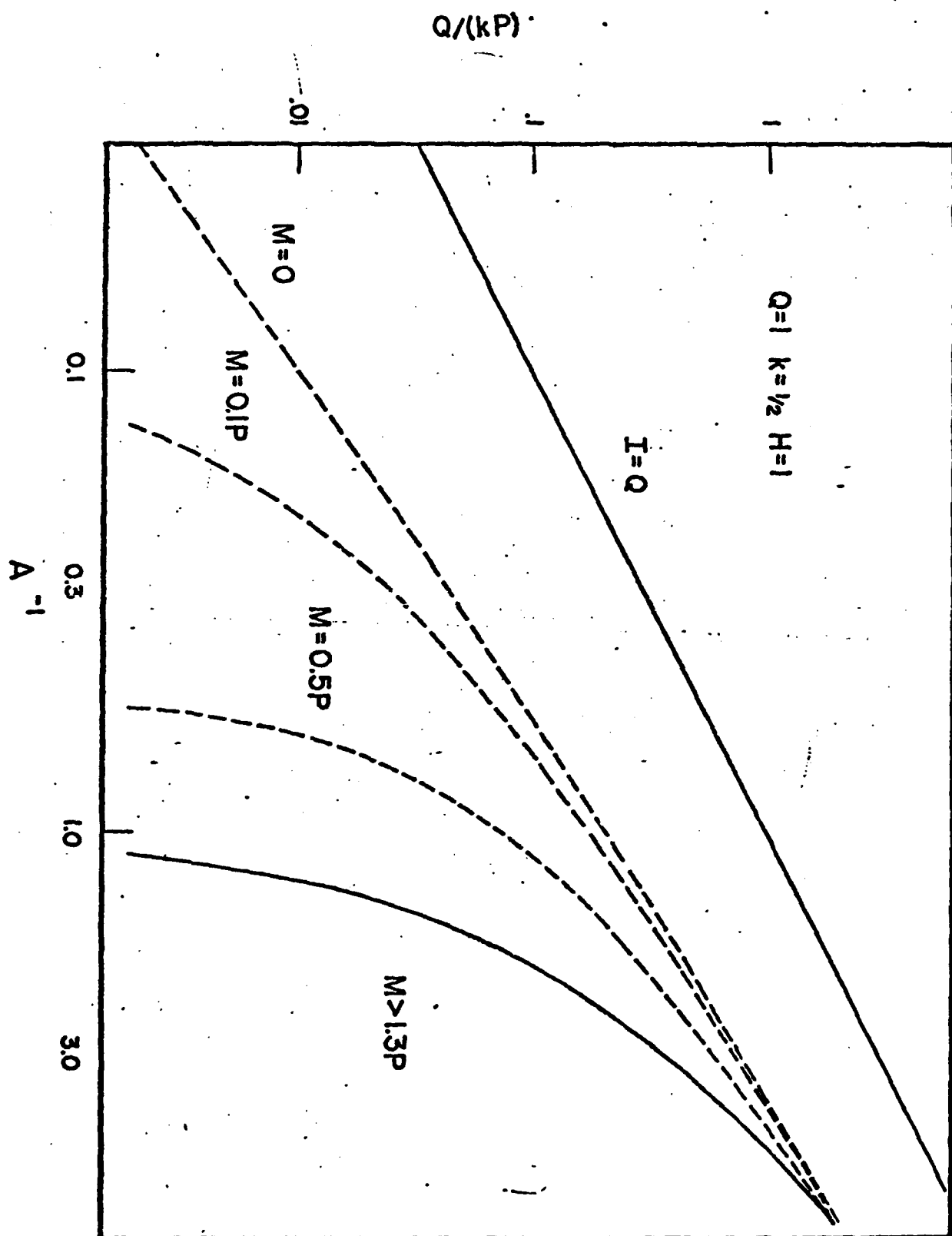
Fig. 6. Wavelengths (in units of D/V) at the onset of instability as a function of $Q/(kP) = [(k_L G_L + k_s G_s)D^2]/[2\bar{k}T_M \Gamma kV^2]$ with $Q = 1$, $k = \frac{1}{2}$, and $M = 0$ for $H = 0$ and $H = 1$. For $H = 0$, the instability is non-oscillatory, and there is only a transverse wavelength (transverse to the growth direction). For $H = 1$, the instability is oscillatory and there are both transverse and longitudinal wavelengths.
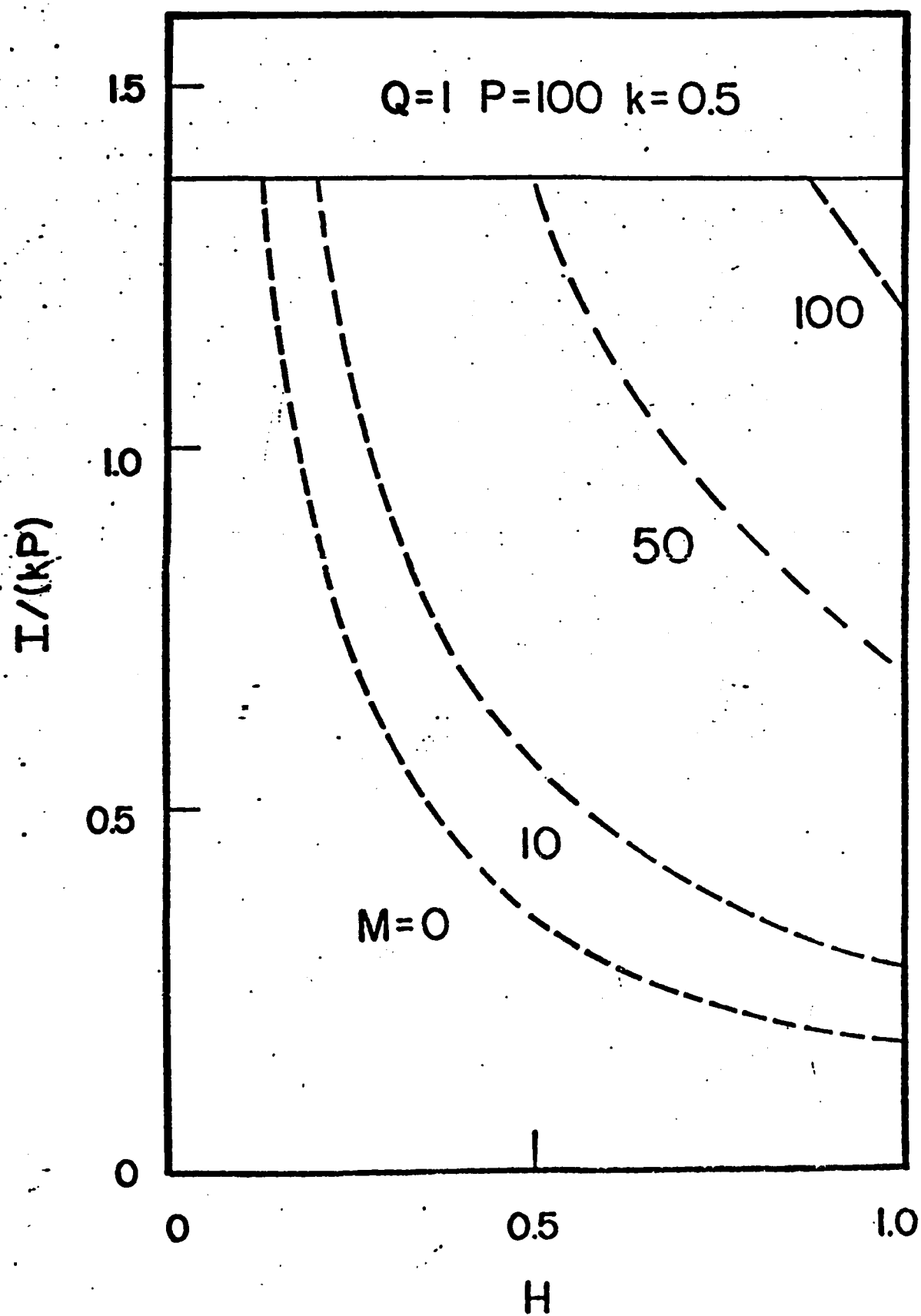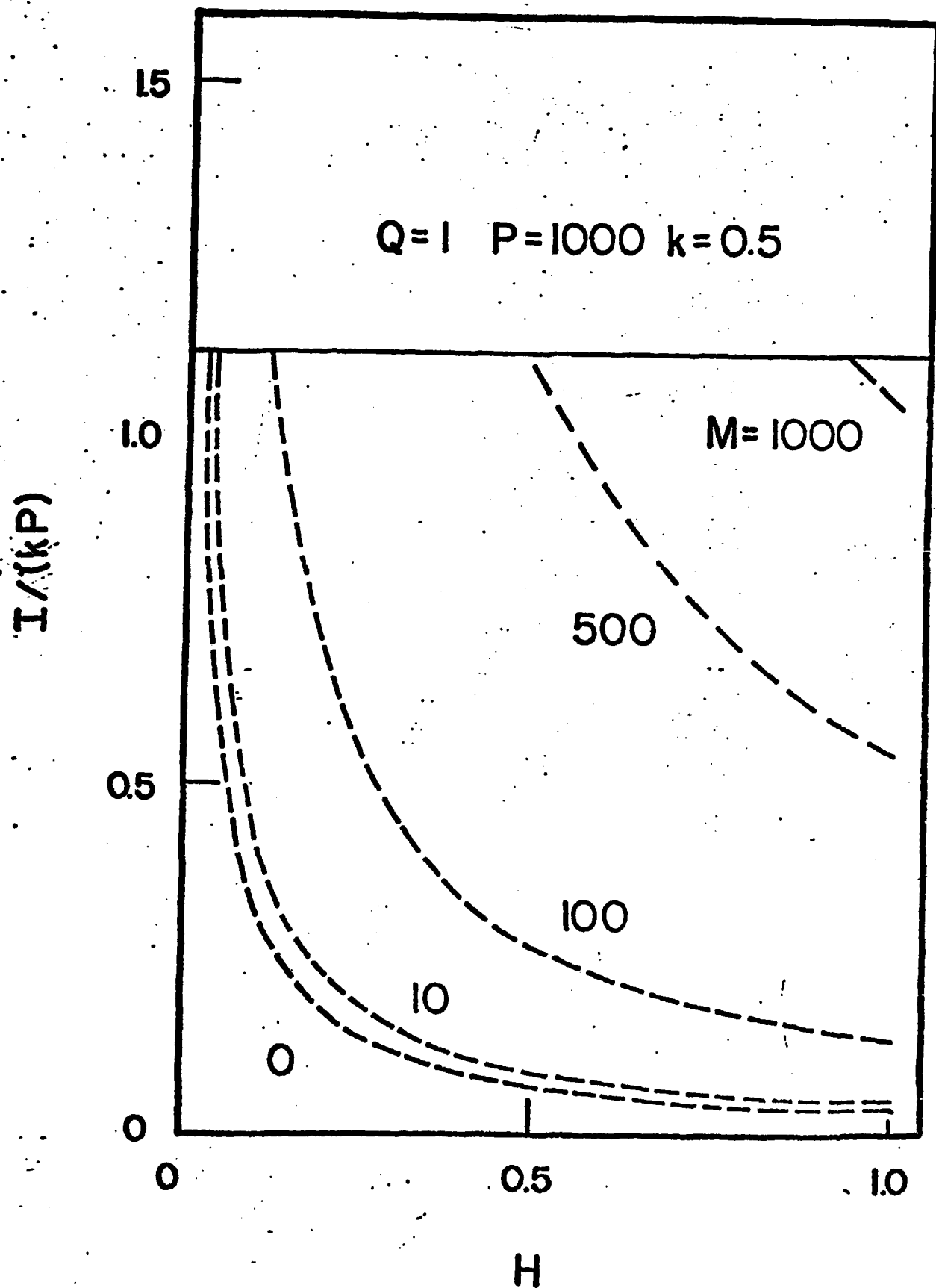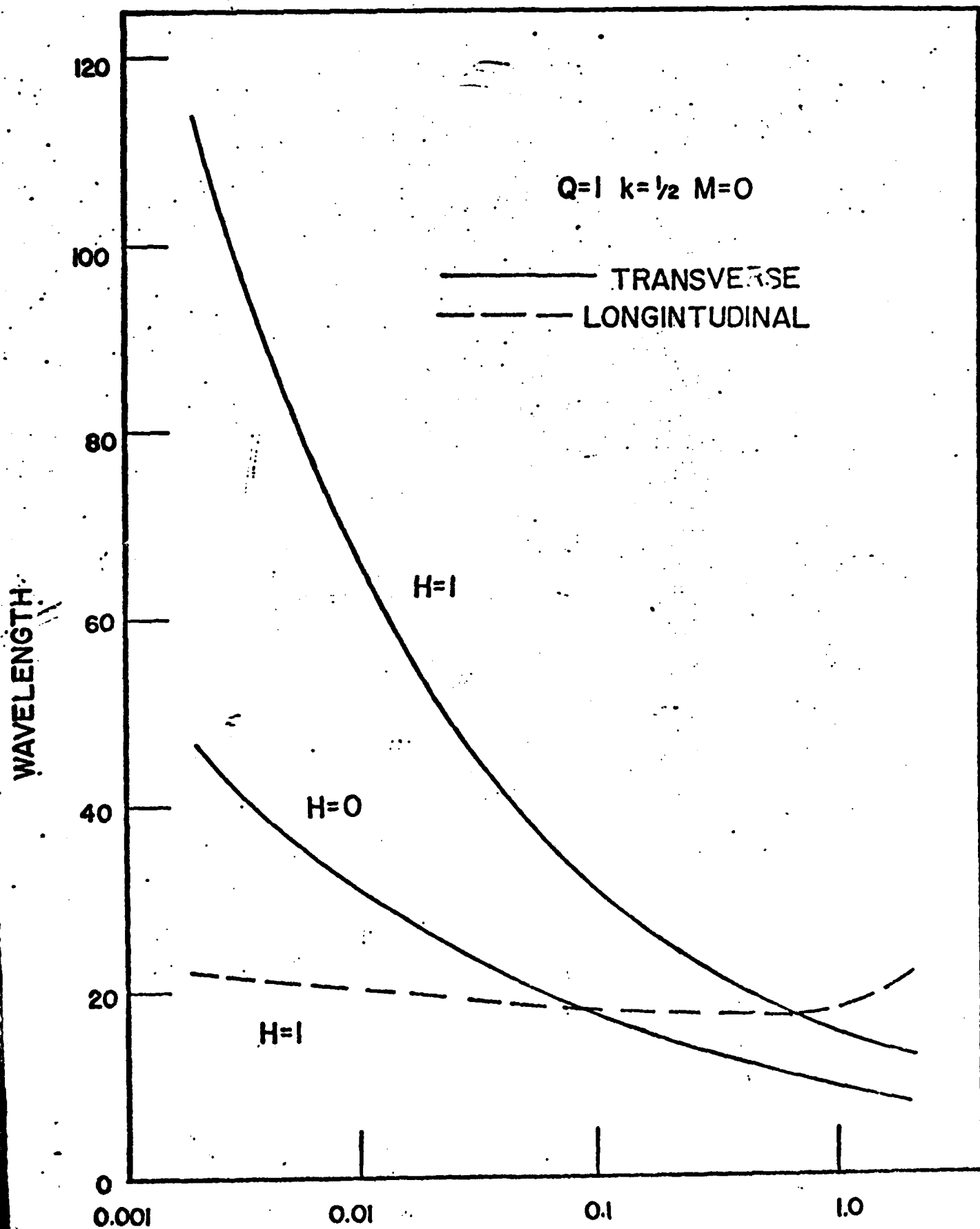
REAL(Σ)

IMAG(Σ)

$\eta$

Q=1 P=1000 k=0.5 I=500
M=H=0

51

REAL ($\Sigma$)

Q=1 P=1000 k=0.5 M=0 I=500

Q=1  k=½  M=0

———————— TRANSVERSE
— — — — LONGINTUDINAL

56

PROCESSING/MICROSTRUCTURE RELATIONSHIPS IN SURFACE MELTING

R. J. SCHAEFER AND R. MEHRABIAN
National Bureau of Standards, Washington, D.C.   20234

## ABSTRACT

The development of predictive models for rapid surface melting and resolidification requires coupling of realistic heat flow models to emerging theories of rapid solidification processing. Attainment of unique microstructures and phases, for example through plane-front solidification and solute trapping, can be correlated to solid/liquid interface velocity, temperature and temperature gradients, and to theories of morphological stability. However, there are important limitations on achievable solid/liquid interface velocity depending upon the heating mode and heat flux distribution, melt thickness and location of the interface within the molten zone.

An overview is given of the emerging guidelines for prediction and control of rapid solidification conditions and microstructures. Homogenization of the liquid by convection and diffusion is also discussed. Electron beam surface melting of alloy substrates is used as an example of these processes.

## INTRODUCTION

The generation of special microstructures through surface melting by directed energy sources is strongly dependent upon the local interface velocities and temperature gradients. In particular, the theory of morphological stability predicts in detail the velocity and gradient dependence of the transition from microscopically planar to non-planar interfaces. The transition from cellular to more complex dendritic interfaces is also influenced by velocities and gradients, but the theory describing this transition is not so well developed, particularly with respect to prediction of special behavior which may arise at rapid rates of solidification.

When a laser or electron beam is used to create a transient melted layer on the surface of a material, the solid-liquid interface experiences a cycle of gradient and velocity conditions as it resolidifies, and a corresponding distribution of microstructures can be predicted. Because the solidification cycle can be altered by selecting different modes of surface heating, such as pulsing or scanning the energy beam, there exists the possibility of altering the distribution of microstructures by altering the heating mode.

We shall describe here these solidification cycles mainly as they apply to the morphological stability theory of the transition from planar to non-planar interfaces, because the quantitative description of this transition is so well developed. The liquid is assumed to be initially homogeneous, and we consider the processes which can eliminate in the liquid the microsegregation which was present in the initial solid.

## INTERFACE STABILITY

During solidification processes in which a positive temperature gradient is present in the liquid and the latent heat of fusion is therefore removed through the solid, plane-front solidification becomes decreasingly stable with increasing growth velocity, so long as the velocity lies in the conventional range of less than about $10^{-3}$ m/s. This trend and the approximate values of the gradient, concentrations, and velocities at which planar interfaces become unstable are predicted by the well-known principle of constitutional super-cooling [1], which is based on the concept that the planar interface becomes unstable if the temperature in a region ahead of the interface is lower than the liquidus temperature as determined by the local solute concentration. This theory predicts that planar interfaces will be stabilized by a temperature gradient in the liquid greater than

$$G_L = mVC_\infty(k-1)/Dk \tag{1}$$

where m is the liquidus slope, V is the solidification velocity, $C_\infty$ is the solute concentration in the liquid far from the interface, k is the equilibrium partition coefficient and D is the solute diffusion constant in the liquid. most crystal growth processes the values of the parameters appearing in this equation can be estimated with reasonable accuracy and the use of the constitutional supercooling concept is therefore widespread. However, morphologic stability analysis [2] of solidification processes has now been available for many years and it not only gives a more detailed description of interfacial behavior, it predicts effects, particularly at rapid solidification velocities which differ dramatically from the behavior expected on the basis of the constitutional supercooling concept. By considering the relatively simple expressions which morphological stability theory predicts under certain limiting conditions, the influence of temperature gradients and interface velocity on the stability is most clearly evident. Considering first a situation in which all effects of interfacial surface energy and kinetics are neglected, the morphological stability analysis predicts a relation very similar to Eq. (1):

$$\frac{G_L k_L + G_S k_S}{k_L + k_S} = \frac{mVC_\infty(k-1)}{Dk} \tag{2}$$

where $k_L$ and $k_S$ are the thermal conductivity of the liquid and the solid, respectively. Recognizing the expression for conservation of heat at the solid-liquid interface,

$$VL = k_S G_S - k_L G_L \tag{3}$$

where L is the latent heat of fusion per unit volume, Equation (2) may also be written

$$\frac{2G_L k_L + VL}{k_L + k_S} = \frac{mVC_\infty(k-1)}{Dk} \tag{4}$$

in which form it becomes clear that for $V \ll 2G_L k_L/L$, the critical concentration for instability at a given $G_L$ is inversely proportional to V,

$$C_\infty = 2G_L k_L Dk/(k_L + k_S)m(k-1)V \tag{5}$$

whereas for $V >> 2G_L k_L/L$ the critical concentration for instability approaches a minimum value

$$C_\infty = LDk/(k_L+k_s)(k-1)m \qquad (6)$$

independent of both $G_L$ and V. The stabilization of the critical concentration at high velocity in this case is a direct result of the steep gradient in the solid which is required to extract the latent heat of fusion. The transition between these regimes occurs at velocities near $V = 2G_L k_L/L$. For a conventional (Czochralski or Bridgman) crystal growth process we might have $G_L = 5 \times 10^3$ K/m and using the properties from Table I we find $V = 8.4 \times 10^{-4}$ m/s for Al and $V = 1.5 \times 10^{-4}$ m/s for Si which is very rapid for such growth processes. When solid-liquid surface energy effects are included the morphological stability expressions become considerably more complex but equation (5) is still valid at small velocities whereas at high velocities a new limiting expression is obtained, which may be referred to as the absolute stability criterion,

$$C_\infty = k^2 T_M \Gamma V/m(k-1)D \qquad (7)$$

where $T_M$ is the melting temperature and $\Gamma$ is a surface energy parameter. Mullins and Sekerka [3] have shown that the critical concentration for morphological instability always lies above this value. Eq. (7) is a manifestation of the increasing tendency of surface energy to retard the growth of perturbations as the wavelength becomes shorter at high velocity. Note that now $C_\infty$ is independent of $G_L$ (although it is assumed that the quantity on the left side of Eq. (2) is positive) and is proportional to V. Eq. (7) therefore predicts, in comparison to the constitutional supercooling criterion or to morphological stability theory without surface energy, an extremely large stabilizing effect at high velocities. The limiting curves given by equations (5) and (7) intersect at the concentration

$$C_\infty = [2T_M \Gamma G_L k_L/(k_L+k_s)]^{1/2} k^{3/2}/m(k-1) \qquad (8)$$

Figures (1) and (2) show morphological stability curves for the solidification of silicon containing arsenic [4] and for aluminum containing silver [5], and the various limiting expressions of equations (1), (5), (6) and (7), computed using the material properties of Table I. A notable difference between these systems is that in the silicon based system the minimum concentration for morphological instability, Eq. (6), is considerably greater than the concentration at which the low velocity limit line, Eq. (5), and the absolute stability line, Eq. (7), intersect, whereas in aluminum this is not true. Thus in the silicon based system (and in other silicon-based systems [4]), the interface is stabilized by the temperature gradients due to latent heat emission before the absolute stability effects of surface energy become strong, whereas in aluminum the absolute stability effects are predicted to occur before the latent heat stabilization becomes significant. This difference is due to the large latent heat of fusion and the rapid solute diffusivity in liquid silicon compared to the values for metallic-based systems. The constitutional supercooling line lies above the low velocity limit of the morphological stability curve in aluminum-based systems and below it in silicon-based systems, because of the relative thermal conductivities of the solid and liquid phases.
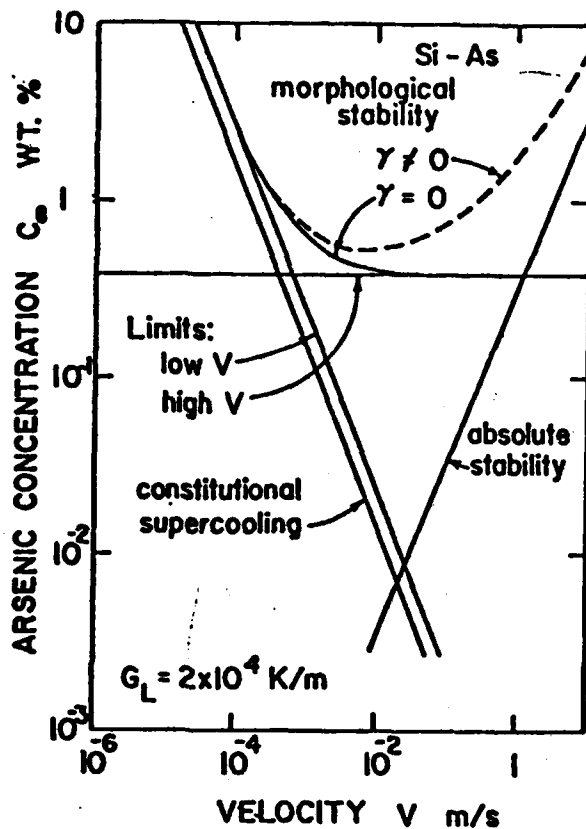
59

Fig. 1. Interfacial stability of Si containing As. The morphological stability curves with (dashed curve) and without (solid curve) surface energy are shown.
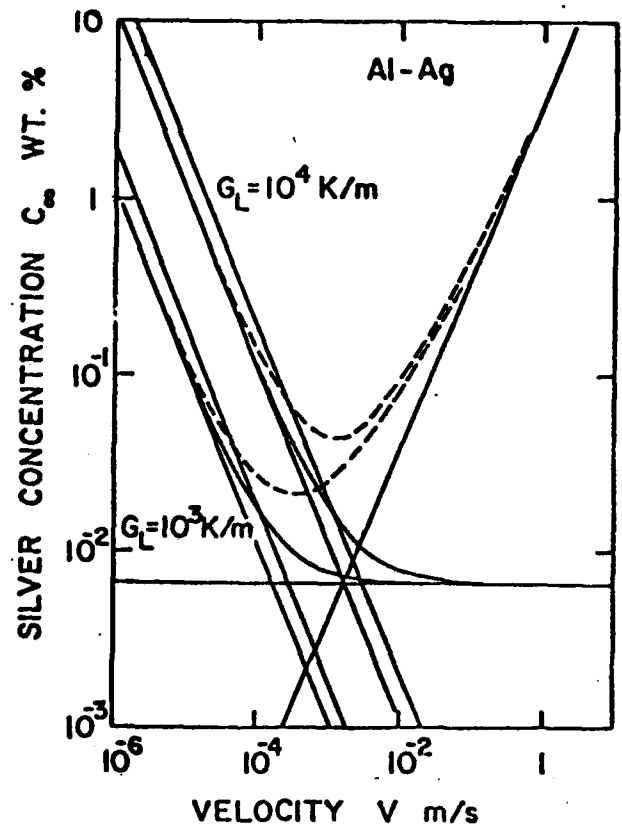
Fig. 2. Interfacial stability for two different gradients in Al containing Ag, showing the same curves as in Fig. 1.

Table I
Properties used in calculations

|  | $k_L$ (J/s·m·k) | $k_s$ (J/s·m·k) | L (J/m³) | $T_M\Gamma$ (m·K) |
|---|---|---|---|---|
| Al | 90.4 | 211 | $1.08 \times 10^9$ | $1.0 \times 10^{-7}$ |
| Si | 70 | 22 | $4.56 \times 10^9$ | $1.3 \times 10^{-7}$ |

|  | k | D (m²/s) | m (K/wt.%) |
|---|---|---|---|
| Al-Ag | 0.41 | $4.5 \times 10^{-9}$ | -1.7 |
| Al-Mn | 0.79 | $2.1 \times 10^{-9}$ | -1.0 |
| Si-As | 0.3 | $3 \times 10^{-8}$ | -1.7 |

At solidification velocities of a few centimeters to a few meters per second, which are attainable by surface melting processes, non-equilibrium effects can be expected at the solid-liquid interface. Specifically it has been shown [6] that the solute distribution coefficient k can deviate from its equilibrium value toward unity at high solidification velocities. Narayan et al. [7] have analyzed the microstructure of laser melted ion implanted silicon and obtained, for isolated experimental points, a good fit to a morphological stability analysis in which a k value equal to that which prevailed at the solidification velocities occuring in their experiments was used. A recent more detailed analysis by Coriell and Sekerka [8], in which a velocity dependent k was used in the derivation of the morphological stability relations, showed that if the velocity dependence of k is sufficiently rapid the onset of interfacial instability may be different from that predicted using the procedure of Narayan et al. Coriell and Sekerka found that deviation of k from its equilibrium value toward unity is not always a stabilizing factor and if the variation of k with velocity is sufficiently rapid, oscillatory instabilities may occur.

The two systems considered in Figure 1 and 2 have similar rather high values of the distribution coefficient k. From Eq. (7) it is seen that at a given velocity the concentration at which absolute stability can be expected is strongly dependent on k. For example, when aluminum solidifies at a velocity of $10^{-2}$ m/s, it is predicted that 2 wt.% Mn (k = .79) is required to produce morphological instability, whereas $5.2 \times 10^{-4}$ wt.% Fe (k = $2.8 \times 10^{-2}$), $8.3 \times 10^{-5}$ wt.% Ni (k = $8 \times 10^{-3}$) or $4.4 \times 10^{-5}$ wt.% Sn (k = $2 \times 10^{-3}$) will be sufficient to cause instability at the same velocity. If, however, the solidification velocity is sufficiently high to cause the very low partition coefficients to rise from their equilibrium values toward unity, the relative influence of the low k elements may be reduced.

The presentation of the morphological stability results in the format shown in Figures 1 and 2 is useful when considering steady state growth processes or when comparing the behavior of alloys with different compositions. During a surface melting process, however, the interfacial velocity and temperature gradients pass through a cycle of values and a presentation such as that shown in Figure 3, which applies to a specific concentration, is more useful. In the gradient vs. velocity presentation the cycle of conditions experienced during a surface melting process can be plotted as a trajectory. If this trajectory completely by-passes the region of predicted morphological instability, one can expect solidification to occur without microsegregation. Strictly, the theory of morphological stability applies to interfaces moving at steady state rather than under transient conditions, but in rapid solidification processes the solute diffusion fields are localized to an extremely thin region close to the interface and they can therefore change very rapidly as the interface accelerates. When a stationary interface starts to freeze at a velocity V, the characteristic distance over which the solute distribution field develops is s = D/kV [1] and for V = $10^{-2}$ m/s we find in Al-Ag that s = $10^{-6}$ m, which is small compared to the melt depths which could produce this solidification velocity. In the next section we will consider some of the gradient and velocity cycles which occur during different types of surface melting operations, and their implications for morphological stability.

To estimate the effect which the velocity dependence of the partition coefficient k' would have on the curves shown in Fig. 3, we can calculate the absolute stability velocities for these curves with the assumption that the velocity dependence of the partition coefficient is given by

$$k' = \frac{k + \dfrac{V\lambda}{D}}{1 + \dfrac{V\lambda}{D}}$$

where $\lambda$ is taken to be approximately 10 interatomic distances. With this formulation we find that the absolute stability limit for Al-1 wt% Ag is reduced from $2.7 \times 10^{-1}$ m/s to $1.8 \times 10^{-1}$ m/s but that the change of the absolute stability limits for the other curves in Fig. 3 is insignificant. Thus experiments at velocities of $10^{-2}$ m/s or less should not be affected by non-equilibrium partition coefficient effects. Where the solidification velocity is sufficiently high that $k' \rightarrow 1$ (solute trapping), partitionless solidification is expected at concentrations considerably greater than given by Eq. (7). This can occur only when the interface temperature is below $T_o$, the temperature at which solid and liquid have the same free energy.

## ATTAINABLE FREEZING PARAMETERS

The combinations of melt depth, solidification velocity, and temperature gradient which can be attained by a surface melting operation are limited by heat flow, but are not identical for all modes of surface heating.

### a) One-Dimensional Heat Flow

A one-dimensinal heat flow situation prevails when the surface is melted by a pulsed energy beam with radius, a, large compared to the distance over which heat can diffuse during the duration t of the pulse, i.e., $a > 4\sqrt{\alpha_s t}$ where $\alpha_s$ is the thermal diffusivity of the solid [9]. This condition commonly occurs during melting by Q-switched lasers or rapidly pulsed electron beams, but is difficult to attain during surface melting by CW lasers or by welding-type electron beams.

A useful characteristic of solidification with one-dimensional heat flow is that after the maximum melt depth has been attained the interface accelerates rapidly to a solidification velocity which remains almost constant until it reaches the surface. During the accelerating phase, the gradient in the liquid drops rapidly from a value which is comparable to the gradient in the solid when the interface velocity is zero at the maximum melt dept, to a value which is negligible compared to the gradient in the solid.

For the case of aluminum Hsu, Chakravarty and Mehrabian [10] found that if the surface is heated to the boiling temperature (2723 K) by a heat flux of intensity q (W/m$^2$) and the heat flux is then removed, the solidification velocity in meters per second is close to $V = 7 \times 10^{-11}$ q after the initial transient which accounts for about 20% of the melt depth. It was found that the maximum melt depth in meters for aluminum heated to its boiling point by a heat flux q is given by $d = 3.3 \times 10^5/q$. Combining these expressions gives $V = 2.3 \times 10^{-5}/d$ as the maximum velocity which may be attained for a surface melt of depth d with one-dimensional heat flow. Melting to the same depth with a lower power density and longer time will give lower velocities.

When the velocities and gradients which occur during solidification with one-dimensional heat flow are represented on the plot of Figure 3, they can completely by-pass the region of morphological instability of a dilute alloy. Near the maximum melt depth $G_L/V$ is large and gradient stabilization is effective, whereas the subsequent precipitous decrease in $G_L$ allows V to become large enough to stabilize the interface through absolute stability effects. Dashed line (a) in Figure 3 shows the velocity-gradient trajectory which occurs during solidification of aluminum following melting to the boiling point by an energy source of intensity $5 \times 10^8$ W/m$^2$.

### b) Pulsed Spot

When a surface is melted by a pulsed energy beam with a diameter which is not large compared to the distance over which heat can diffuse during the length of the pulse, the relationships between solidification velocity, melt depth and
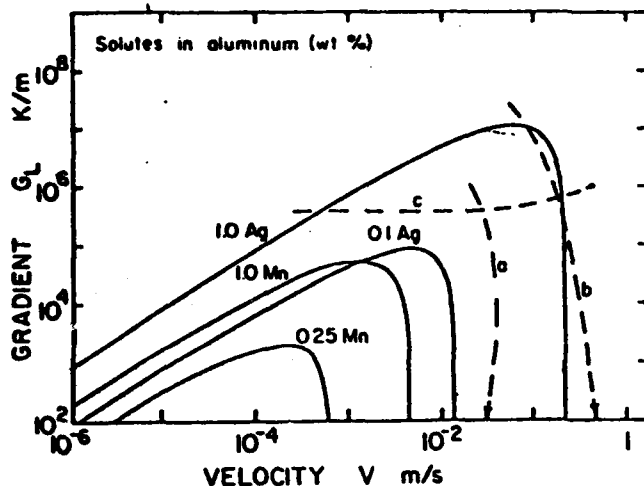
62

Fig. 3. Morphological stability of Al containing Ag or Mn. The region of instability lies below the curves. Dashed lines show trajectories for a) one-dimensional, b) pulsed spot and c) moving spot melts.

absorbed power density are not as simple as in the one-dimensional case [9].

When a spot of radius a is heated by a uniform absorbed energy of intensity q the surface temperature at the center of the heated zone rises toward a steady state value which is approached very closely at a time $t = a^2/0.16\alpha_s$, which for the case of a 1 mm diameter spot on aluminum is 18 milliseconds. The temperature reached at the center of the spot at steady state is determined by the product qa, which must have a minimum value of $2.3 \times 10^5$ W/m to initiate surface melting in aluminum and a value of $4.2 \times 10^5$ W/m to bring the surface to the vaporization temperature at the center of the spot.

Melting by means of a pulsed spot allows solidification at a given velocity from a greater depth than is possible with one-dimensional heat flow. For example if $qa = 4.2 \times 10^5$ W/m and $a = 5 \times 10^{-4}$ m, the maximum melt depth is $3.25 \times 10^{-4}$ m and the velocity of solidification rises from zero at the bottom of the pool to $10^{-1}$ m/s by the time the depth has decreased 5 percent. The interface then accelerates steadily to a velocity of almost 0.4 m/s as it approaches the surface. For the one-dimensional heat flow case a melt of the same depth would resolidify with an almost constant velocity of about $7 \times 10^{-2}$ m/s (see Fig. 4).

Just as in the case of one-dimensional heat flow, the superheat in the liquid pool established by the pulsed spot diminishes rapidly after the heat source is turned off, and the gradient in the liquid becomes much smaller than that in the solid.
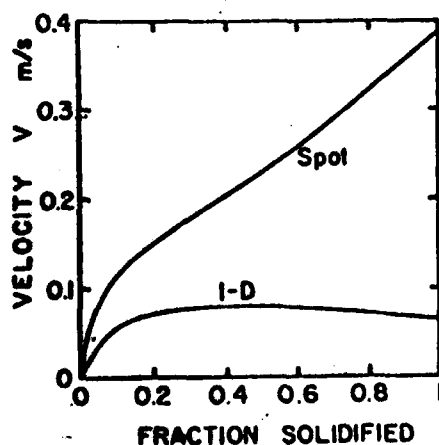


Fig. 4. Solidification velocities following melting to a depth of 3.25 $\times 10^{-4}$ m by a pulsed spot with qa = $4.28 \times 10^5$ W/m and by one-dimensional heat flow.

63

For a pulsed spot melt, the gradients and velocities depend upon the location within the pool and the trajectory shown on a plot such as Figure 3 will be different for material growing straight up along the central axis of the pool when compared to that for material growing radially inward from the edges. Moreover, the maximum velocity of solidification in this type of melt develops only after the gradient in the liquid has fallen to a value much less than that which was present when solidification started. Typical trajectories may thus enter a region of instability and then pass into the absolute stability regime, as illustrated schematically by dashed curve (b) in Figure 3. For such cases it is important to make the distinction that morphological stability theory predicts the conditions under which a planar interface will become unstable but does not consider the conditions required for a cellular or dendritic interface to revert to a planar morphology. Thus there is no theoretical basis on which to predict that the maximum velocities experienced in the final stages of solidification after melting by a pulsed spot will result in microsegregation-free solid, if a region of instability has been encountered earlier in the process. To avoid morphological instability the critical region for the pulsed spot will be near the bottom of the melt pool where the interface has not reached its maximum velocity, but the gradient has decreased substantially. Even in this reigon, however, the velocity is higher than that obtainable with one-dimensional heat flow in a melt of the same depth.

### c) Moving Spot

When a melt pool is established by a spot of directed energy moving across a surface of velocity $U$, the local solidification velocity is $U \cos\theta$, where $\theta$ is the angle between the normal to the interface and the direction of motion of the energy spot. Thus the interface velocities, which are always less than the velocity of motion of the spot, depend at steady state only on the location within the cross section of the melt and not on the position along the melt trail. Correlation of metallographically observed microstructures to local interface velocities is therfore relatively easy. In this situation the sequence of velocities and gradients experienced by the solid-liquid inteface are those lying along the line traced out by the normal to the interface as the melt pool moves. The shape of this line may often be deduced from observation of aligned microstructures in a longitudinal section of the melt.

Thermal analysis of the moving spot [11] is based on the parameters qa and $Ua/2\alpha$. When $Ua/2\alpha \ll 1$, the shape of the melt pool differs little from the steady state pool shape at $U = 0$, but as $Ua/2\alpha$ approaches unity the melt pool distortion becomes significant.

In this mode of melti g the gradients in the liquid do not become very small as they do in the modes discussed above, because here the heat source is applied continuously. The value of $G_L/V$ at the solidifying interface is shown for different values of qa and $Ua/2\alpha$ in [11] where it is seen that $G_L/V$ decreases from infinity at the bottom of the pool (where $V = 0$) to a minimum value at the trailing edge of the pool (where $V$ has its maximum value). The minimum value of $G_L/V$, at a given qa level, becomes larger as $Ua/2\alpha$ becomes smaller: when $Ua/2\alpha \ll 1$ and the shape of the melt pool is essentially independent of $Ua/2\alpha$, the minimum value of $G_L/V$ is inversely proportional to $U$. Fig. 3 shows a trajectory (c) obtained with this type of melt for qa = 6.4 x $10^5$ W/m, $a = 5 \times 10^{-4}$ m, and $Ua/2\alpha = 0.75$.

### HOMOGENIZATION OF THE MELT

Most surface melting processes will be carried out on materials which initially are microsegregated. The time in the liquid phase will in general be too short to allow elimination of this inhomogeneity by diffusion. An exception to this situation is possible with the pulsed spot, in which case the melt

pool and thermal field reach a steady state configuration and if it is within the capability of the energy source the liquid phase may be held as long as desired to complete homogenization. For the case of a moving spot, if we estimate a diffusion distance $(Dt)^{1/2}$ for a melt pool 1 mm long we find that Ag in Al would move about 20 µm by diffusion in a melt moving at $10^{-2}$ m/s and only about 3µm in a melt moving at 0.5 m/s. In the latter case many microsegregation patterns would be diminished insignificantly by diffusional homogenization.

There is, however, abundant evidence that convection can be vigorous in the melt pools generated by directed energy sources. The surface topography features which are often present after melting have been attributed to the effect of this fluid flow [12]. A vigorous flow pattern can be expected to result from the influence of the temperature-dependent liquid surface energy (Marangoni convection) because gradients on the liquid surface can easily exceed $10^6$ K/m. In addition, when a plasma is formed above the metal surface, the increased roughness of the surface suggests that a still more vigorous agitation of the fluid is present. In the next section we present some experimental evidence of the action of convective flow.

## SURFACE MELTING OF ALUMINUM ALLOYS

We have used electron beams to melt the surface of aluminum alloys containing Ag and Mn, which have high partition coefficients and therefore should produce morphological instability only when present in relatively high concentrations. In pulsed spots and moving spots it is found that a microsegregation-free zone is present at the bottom of the melt pool but that cellular microstructure is present above this region even at velocities several times greater than those predicted to be required to produce absolute stability. The microsegregation-free zone is the region where $G_L/R$ is highest but because there must be at least some growth of the solid between the place where the planar interface becomes unstable and the place where a metallographically visible cellular structure has developed, it is difficult to determine the exact $G_L/R$ value at which the interface becomes unstable.

The most probable cause of the cellular substructure in aluminum alloys containing the high k solutes Ag and Mn at velocities where absolute stability was expected is the presence of much lower concentrations of elements with much lower k values. A concentration of 1-5 ppm of Fe or Ni would be sufficient to cause instability in the velocity range (approximately $10^{-2}$ to 0.3 m/s) which was investigated, but would be difficult to determine in a small zone especially in the presence of a large concentration of Mn.

It has been known for many years [13] that rapidly solidified Al-Mn alloys can contain Mn in solid solution far beyond the maximum equilibrium concentration of ~1.8 wt%. X-ray diffraction patterns of electron beam surface melted samples show at 7 wt.% Mn only a faint trace of second phase material present. This alloy appears to supersaturate so readily that the concentration differences resulting from cellular solidification are small and in many cases difficult to reveal. Electrolytic etching in a solution of 40% nitric acid and 60% methanol was found to be most effective at revealing cellular structures in these alloys.

While elements such as Fe or Ni might be responsible for causing the interface to become cellular, the microstructure becomes visible only because of the much higher concentration of Mn or Ag which also becomes segregated to the cell boundaries.

In some cases a swirled fluid flow pattern was frozen into the melt zone, which on close examination was revealed as differences in the cell spacing or pattern. These differences appeared to be remnants of the much larger scale cellular segregation pattern which was present in the arc melted substrate.

To obtain an indication of the rate at which mixing and homogenization occur in the melt zone, a thin Cu wire was pressed into the surface of a block of Al and reacted at slightly above the eutectic temperature to produce when it cooled a thin band containing primary Al in a eutectic matrix. The sample surface was then melted by electron beam spots $10^{-3}$ m in diameter moving perpendicular to the alloyed band at different power levels and velocities. Figures 5 through 8 show some of the results of this operation as seen on a polished section lying slightly below the original sample surface.

In Figure 5 the scan speed of the electron beam was $2 \times 10^{-2}$ m/s. The power level was not sufficient to melt the pure Al at the plane of the section (although it did melt the surface) but the eutectic within the alloyed zone was melted and resolidified with a much finer lamellar structure. The lighter regions within the melt zone, streaming away from the large primary particles, contain a large volume fraction of finely divided primary phase. These streams can be seen to have carried material at least 200 µm during the approximately $5 \times 10^{-2}$ s that the material was molten which implies that the flow velocity was at least $4 \times 10^{-3}$ m/s, but possibly much larger because one cannot tell if the streams have merely dissipated beyond 200 µm in the melt.

With the same power level but ten times the scan velocity, there is little evidence of fluid flow (Fig. 6). The eutectic has been melted and refined in scale but the primary particles show only a shadowing around their perimeters which at higher magnification appears to be due to a partial melting in the form of numerous very small droplets. Thus the melting of the primary particles was insufficient to delineate any fliud flow which may have been present.

At higher power levels the fluid flow effects are much more conspicuous. In Figure 7, in which the electron beam was scanned at $2 \times 10^{-2}$ m/s, all of the primary in the melt zone except that very close to the edges has been melted and thoroughly mixed. Copper has been transported upstream at least $10^{-3}$ m implying a fluid flow velocity of at least $2 \times 10^{-2}$ m/s.

Figure 8 shows the result of scanning the beam at 0.2 m/s and here it is seen that although considerable fluid flow has taken place there has been insufficient time to thoroughly homogenize the molten zone. In this case the upstream motion of $10^{-3}$ m implies a fluid flow velocity of at least 0.2 m/s.

From these observations one can set the lower bounds on the fluid flow velocity, but one derives little information on upper bounds. It is clear that convective mixing is an important part of melt homogenization in microsegregated substrates. It will certainly play a dominant role in surface alloying [14].
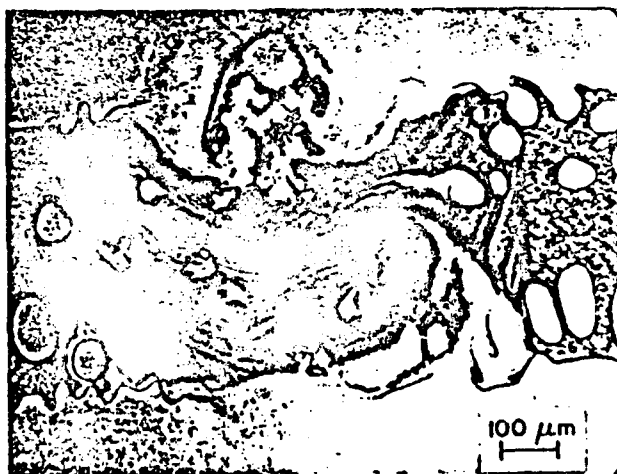


100 µm

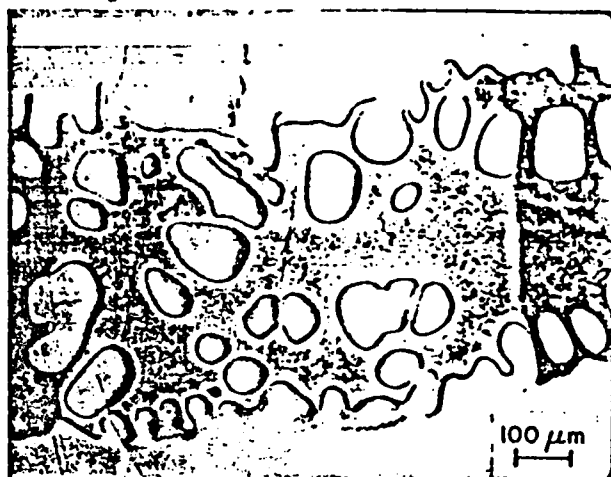Fig. 5. Electron beam scan at $2 \times 10^{-2}$ m/s across Al-Cu eutectic band in Al.

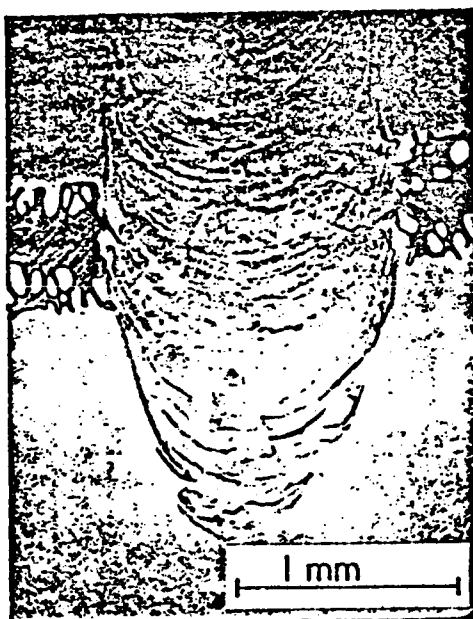Fig. 6. Electron beam scan at 0.2 m/s across eutectic band.



Fig. 7. Electron beam scan at $2 \times 10^{-2}$ m/s across eutectic band.



Fig. 8. Electron beam scan at 0.2 m/s across eutectic band.

## SUMMARY

The temperature gradient and interface velocity cycles which occur during different modes of surface melting are the most important controlling paramet in the determination of solidification microstructures. These cycles can be related to the conditions predicted to cause microstructural transitions, the best developed of which is the theory of morphological stability of planar interfaces. This theory predicts increasing stability at sufficiently high rates of solidification, but clear evidence of this effect has been observed only at velocities so high that the deviation of the solute partition coeffi cient from its equilibrium value plays an important role.

To obtain the ideal microstructures predicted by solidification theory the melt zone must be homogeneous. Convection plays a leading role in the elimination of the residual microsegregation patterns from the substrate. Complete homogenization may require a slow melt for homogenization followed by a faster melt for the final microstructural refinement.

## ACKNOWLEDGMENTS

## REFERENCES

1. W. A. Tiller, J. W. Rutler, K. A. Jackson and B. Chalmers, Acta Met. 1, 428 (1953).

2. W. W. Mullins and R. F. Sekerka, J. Appl. Phys. 34, 323 (1963)

3. W. W. Mullins and R. F. Sekerka, J. Appl. Phys. 35, 444 (1964).

4. J. W. Cahn, S. R. Coriell, and W. J. Boettinger in: Laser and Electron Beam Processing of Materials, C. W. White and P. S. Peercy eds. (Academic Press, New York 1980) pp. 89-103.

5. R. J. Schaefer, S. R. Coriell, R. Mehrabian, C. Fenimore and F. S. Biancaniello in: Rapidly Solidified Amorphous and Crystalline Alloys, B. H. Kear, B. C. Giessen and M. Cohen eds. (North-Holland, New York 1982) pp. 79-89.

6. C. W. White, S. R. Wilson, B. R. Appleton and J. Narayan in: Laser and Electron Beam Processing of Materials, C. W. White and P. S. Peercy eds. (Academic Press, New York 1980) pp. 124-129.

7. J. Narayan, J. Crystal Growth 59, 583 (1982).

8. S. R. Coriell and R. F. Sekerka, J. Crystal Growth (in press).

9. S. C. Hsu, S. Kou and R. Mehrabian, Met. Trans. 11B, 29 (1980).

10. S. C. Hsu, S. Chakravorty and R. Mehrabian, Met. Trans. 9B, 221 (1978).

11. S. Kou, S. C. Hsu and R. Mehrabian, Met. Trans. 12B, 33 (1981).

12. S. M. Copley, D. G. Beck, O. Esquivel and M. Bass in: Lasers in Metallurgy, K. Mukherjee and J. Mazumder eds. (The Metallurgical Society of AIME, Warrandale, Pa. 1981) pp. 11-19.

13. G. Falkenhagen and W. Hofmann, Z. Metallkunde 43, 69 (1952).

14. C. W. Draper, Journal of Metals 34, No. 6, 24 (1982).